NeuroImage 202 (2019) 116087

Contents lists available at ScienceDirect

NeuroImage

journal homepage: www.elsevier.com/locate/neuroimage

Ultra-high resolution and multi-shell diffusion MRI of intact ex vivo human brains using k_T-dSTEAM at 9.4T

F.J. Fritz *, S. Sengupta, R.L. Harms, D.H. Tse, B.A. Poser *, A. Roebroeck *

Department of Cognitive Neuroscience, Faculty of Psychology and Neuroscience, Maastricht University, Maastricht, the Netherlands

ARTICLE INFO

Keywords:
Diffusion MRI
Ex vivo human brain
k_T-dSTEAM
Ultra-high field MRI

ABSTRACT

Diffusion MRI (dMRI) in ex vivo human brain specimens is an important research tool for neuroanatomical investigations and the validation of dMRI techniques. Many ex vivo dMRI applications have benefited from very high dMRI resolutions achievable on small-bore preclinical or animal MRI scanners for small tissue samples. However, the investigation of entire human brains post mortem provides the important context of entire white matter (WM) network systems and entire gray matter (GM) areas connected through these systems. The investigation of intact ex vivo human brains in large bore systems creates challenges due to the limited gradient performance and transmit radio-frequency (B_1+) inhomogeneities, specially at ultra-high field (UHF, 7T and higher). To overcome these issues, it is necessary to tailor ex vivo diffusion-weighted sequences specifically for high resolution and high diffusion-weighting. Here, we present k_T-dSTEAM, which achieves B_1+ homogenization across whole human brain specimens using parallel transmit (pTx) on a 9.4T MR system. We use k_T-dSTEAM to obtain multi-shell high b-value and high resolution diffusion-weighted data in ex vivo whole human brains. Isotropic whole brain data can be acquired at high b-value (6000–8000 s/mm^2) at high resolution (1000 μm) and at moderate b-value (3000 s/mm^2) at ultra-high isotropic resolution (400 μm). As an illustration of the advantages of the ultra-high resolution, tractography across the WM/GM border shows less of the unwanted gyral crown bias, and more high-curvature paths connecting the sulcal wall than at lower resolution. The k_T-dSTEAM also allows for acquisition of T_1 and T_2 weighted images suitable for estimating quantitative T_1 and T_2 maps. Finally, multi-shell analysis of k_T-dSTEAM data at variable mixing time (TM) is shown as an approach for ex vivo data analysis which is adapted to the strengths of STEAM diffusion-weighting. Here, we use this gain for multi-orientation modelling and crossing-fiber tractography. We show that multi-shell data allows superior multiple orientation tractography of known crossing fiber structures in the brain stem.

1. Introduction

Diffusion MRI (dMRI) in ex vivo human brain specimens is an important research tool for neuroanatomical investigations and for the validation of dMRI techniques. For instance, ex vivo dMRI studies have focused on validation of white matter orientation estimates (Leergaard et al., 2010; Seehaus et al., 2015), microstructure models (Assaf et al., 2008; Leergaard et al., 2010; Mollink et al., 2017) and tractography (Roebroeck et al., 2008; Seehaus et al., 2013), as well as the atlasing and mapping of human subcortical structures (Aggarwal et al., 2013; Dell'Acqua et al., 2013) and the delineation of gray matter layers (Aggarwal et al., 2015; Bastiani et al., 2016; Kleinnijenhuis et al., 2013; Leuze et al., 2014). All ex vivo applications benefit from high (1000 μm isotropic and far below) dMRI resolution, which is difficult to achieve primarily because of two effects. First, since post mortem tissue possesses strongly reduced diffusivity compared to in vivo tissue, the required b-values for diffusion analysis must be proportionally higher, often at least doubled (D'Arceuil et al., 2007; Miller et al., 2012b). Second, the strongly reduced T_2 of fixed tissue (Pfefferbaum et al., 2004) means T_2-weighted signal is lower and signal-to-noise ratio (SNR) is substantially reduced, especially for relatively long echo times (TEs). Ex vivo dMRI using the pulsed gradient spin echo (PGSE) sequence, which is the most common dMRI pulse sequence, is especially challenged due to the strong interaction of both these effects. Using high b-values with PGSE to compensate the lower diffusivity inherently implies longer TE's, and therefore strong signal decay.

---

* Corresponding authors. Department of Cognitive Neuroscience, Faculty of Psychology and Neuroscience, Maastricht University, 6229 EV, Maastricht, the Netherlands.

E-mail addresses: f.lagosfritz@uke.de (F.J. Fritz), benedikt.poser@maastrichtuniversity.nl (B.A. Poser), a.roebroeck@maastrichtuniversity.nl (A. Roebroeck).

https://doi.org/10.1016/j.neuroimage.2019.116087
Received 11 June 2019; Accepted 8 August 2019

Nonetheless, high quality ex vivo dMRI results can be achieved with PGSE on small-bore preclinical or animal MRI systems (e.g. Aggarwal et al., 2015; Calabrese et al., 2015; Fatterpekar et al., 2002; Glover et al., 1994; Nabuurs et al., 2011; Roebroeck et al., 2008; Seehaus et al., 2013; Utz and Monazami, 2009), where post mortem tissue dMRI has so far been predominantly performed. This is due to the superior gradient performance of small-bore preclinical systems, often exceeding five times that of large-bore systems, allowing short-TE/high-b PGSE acquisitions. In addition, ex vivo imaging often involves scanning post-mortem tissue over long scan sessions (many hours to a couple of days) yielding ultra-high resolution datasets far below the millimeter scale while maintaining a sufficiently high SNR for the acquired images. However, the use of small-bore systems is often limited to small human tissue samples (often less than about $20 \times 20 \times 20\,\mathrm{mm}^2$, and generally smaller than about $50 \times 50 \times 50\,\mathrm{mm}^2$), severely restricting the size of the brain region examined.

Here we consider the investigation of entire formalin fixed human brains or hemispheres post mortem to provide the important context of entire white matter (WM) network systems and entire grey matter areas connected through these systems. Since the acquisition of ex vivo dMRI for intact samples of this size necessarily has to take place in large bore systems, this re-introduces the challenge of limited gradient performance compared to small bore systems, and the relative inefficiency of PGSE. Therefore, it is necessary to find and optimize other diffusion-weighted sequences for high resolution and high diffusion-weighting for this specific case. Earlier work by Miller et al. (2012b) and Foxley et al. (2014) has shown that the use of diffusion-weighted Steady State Free Precession (DW-SSFP) for dMRI acquisition of the whole brain ex vivo at 3T and 7T achieves much better SNR efficiency than PGSE. Additionally, the use of ultra-high field (UHF) strength of 7T with DW-SSFP was shown to further increase SNR efficiency and contrast-to-noise ratio (CNR) for whole brain ex vivo dMRI acquisitions, in comparison to 3T. However, a disadvantage of the DW-SSFP sequence is that the signal has a complex dependence on diffusion weighting, T_1, T_2, and flip angle (Buxton, 1993; McNab et al., 2009), making its analysis difficult, especially in the case of multi-shell acquisitions.

Therefore, we consider here the diffusion-weighted STimulated Echo Acquisition Mode (dSTEAM) sequence (Merboldt et al., 1991). The dSTEAM pulse sequence can create a large part of its diffusion contrast during the slower T_1 decay (i.e. during the mixing time while the spins are stored in the longitudinal axis), rather than during the faster T_2 decay. This is advantageous because it overcomes the challenges already mentioned for post mortem whole brain imaging: shortened T_2 and required high b-values. In addition, since T_1 increases and T_2 decreases with increasing field strength, this advantage of dSTEAM is amplified at UHF. Compared to a PGSE acquisition, the main disadvantage of dSTEAM is that it uses only half of the total signal available for the stimulated echo (STE) signal. An effective use of dSTEAM for whole brain post mortem dMRI, then, depends on compensating the need to work with half of the signal with its beneficial effects in the case of UHF ex vivo imaging with low-performing gradients. One general complication of working with large samples at UHF is that B_1+ inhomogeneity is enhanced, which negatively affects the contrast and signal homogeneity of the acquired data. For instance, at 9.4T the required RF excitation wavelength is approximately 8 cm (in brain tissue this wavelength is shorter due to its relative permittivity) which leads to destructive interferences along a whole brain specimen. In the case of dSTEAM, the combination of three consecutive pulses required to obtain the desired STE signal means that B_1+ inhomogeneities are exacerbated to about the third power of those in single excitation sequences (Fig. 1). In gradient recalled echo (GRE) sequences, it has been shown that the B_1+ inhomogeneity can be compensated by replacing the non-selective rectangular excitation pulse by a composite pulse created using the k_T-points method (Cloos et al., 2012), applied in (Sengupta et al., 2018) for post mortem tissue. Therefore, extending the k_T-points B_1+ homogenization method to the more complex three-pulse situation of dSTEAM would potentially create an effective large field of view (FoV) dSTEAM imaging method.

In this work, we address the following objectives for large human brain sample ex vivo dMRI: First, we achieve B_1+ homogenization across whole human brain specimens using parallel transmit (pTx) on a 9.4T MR system by integrating the k_T-points technique in the three-pulse dSTEAM sequence, creating k_T-dSTEAM. Second, we use the k_T-dSTEAM sequence to obtain multi-shell high b-value diffusion-weighted data (6000–8000 s/mm^2) at high resolution (1000 µm) and moderate b-value diffusion-weighted data (3000 s/mm^2) at ultra-high isotropic resolution (400 µm), as well as T_1 and T_2 weighted STEAM images suitable for estimating quantitative T_1 and T_2 maps. Finally, we perform T_1-compensated multi-shell diffusion modeling using k_T-dSTEAM data using the estimated quantitative T_1 maps. We illustrate how ultra-high resolution (400 µm isotropic) whole brain data can benefit tractography at the white matter/gray matter border and how multi-shell multi-orientation analysis can benefit delineation of crossing fibers in deep white matter.

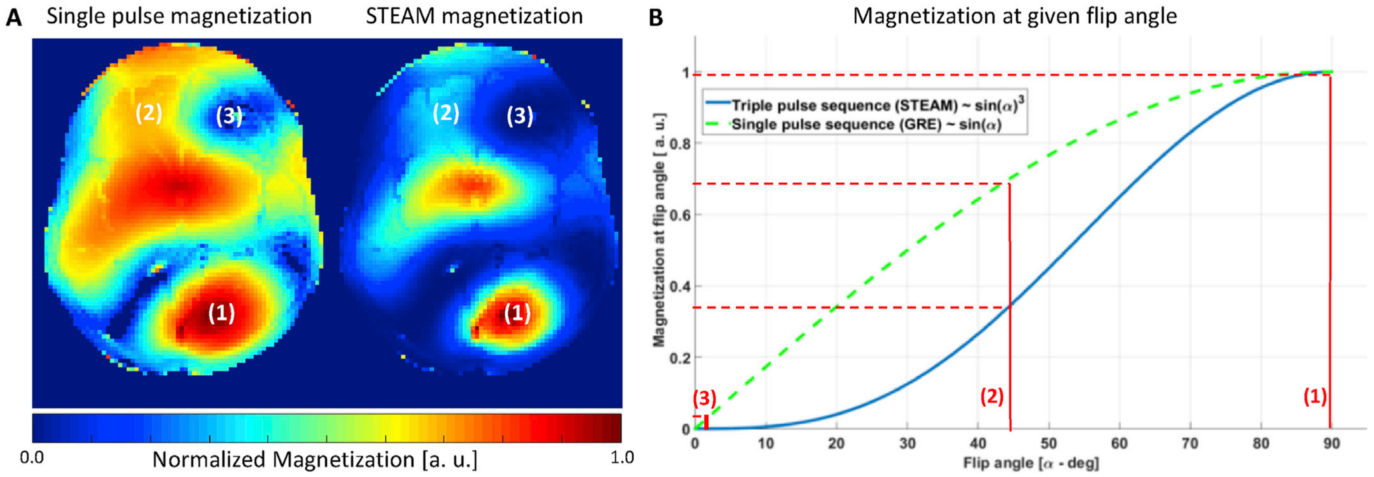

Fig. 1. Amplified signal loss due to B_1^+ inhomogeneities at UHF in STEAM. A) Magnetization for a single pulse sequence (proportional to sin(α)) and for STEAM (proportional to sin(α)^3) derived from a whole human brain flip angle map at 9.4T. Transverse slice with anterior at the top. B) Magnetization plotted as a function of flip angle α for a single pulse sequence (dashed green line, plotted as sin(α)) and for STEAM (solid blue line, plotted as sin(α)^3). Flip angles for location 1, 2 and 3 in A) are indicated. Dashed red lines indicate the corresponding magnetization for location 2 in both single pulse sequences and STEAM.

2. Methods

2.1. k_T-dSTEAM sequence and B_1^+ inhomogeneity

The STEAM pulse sequence uses three RF pulses: excitation, storing and recalling pulses, which can create several spin echos (SEs) and a stimulated echo (STE), and was first introduced by Frahm and colleagues (Frahm et al., 1985). In general terms, the excitation pulse places the magnetization into the transverse plane where it undergoes T_2 decay. After that, the storing pulse places ('stores') part of the total magnetization along the longitudinal axis where it is subject to T_1 decay during the mixing time (TM). The remaining part of the magnetization forms the primary SE signal. Finally, the recalling pulse places ('recalls') the stored magnetization to the transverse plane where it once again undergoes T_2 decay until the STE is formed. This sequence can actually create three more SE echoes (the second, third and fourth spin echo) after the STE, which are consequence of the free induction decay (FID) signal generated by the storing and recalling pulses (Bernstein et al., 2004). We focus on the first or primary SE signal in the remainder of this work and refer to it simply as 'the SE' hereafter. Whereas the SE undergoes only T_2 decay, the STE signal undergoes both T_1 and T_2 decay, because the signal is obtained from spins *stored* along the longitudinal axis for the duration of the TM, making the spins relax under a T_1 regime during this time (see Liang and Lauterbur (1999) for more detail). Furthermore, both echoes (SE and STE) share the transverse magnetization created by the excitation pulse and therefore split the total excited signal, which becomes evenly distributed between SE and STE when the storing pulse has a flip angle of $\pi/2$ rad (90°). The resulting magnitude signal of the STE after excitation in an on-resonance condition (Liang and Lauterbur, 1999) is defined as:

$$S_{STE}(TR,TM,TE,\alpha_i)=\frac{1}{2}\sin(\alpha_1)\sin(\alpha_2)\sin(\alpha_3)\exp\left(-\frac{TM}{T_1}\right)\exp\left(-\frac{TE}{T_2}\right) \tag{1}$$

Here α_1, α_2, and α_3 (α_i in general) are the flip angles of excitation, storing and recalling pulses, respectively. From equation (1), it is clear that the maximum signal for STE is achieved when all the flip angles are $\pi/2$ rad (90°). Due to the three multiplicative flip angle components in the signal, any B_1+ inhomogeneity will greatly affect the resulting signal as illustrated in Fig. 1. Here, for illustration, magnetization (i.e. signal disregarding relaxation decay) for a single pulse sequence, such as GRE (proportional to $\sin(\alpha)$) and for a STEAM sequence (proportional to $\sin(\alpha)^3$) is derived from an actual post mortem human brain flip angle map at 9.4T. In UHF scanners, high B_1+ inhomogeneity over large samples causes signal attenuation and even complete signal loss in some areas. The signal loss and drop-out are already well visible in a single pulse sequence (Fig. 1A, left), but can be considerably amplified in the three pulse STEAM sequence (Fig. 1A, right). Plotting the $\sin(\alpha)$ single pulse magnetization and the $\sin(\alpha)^3$ STEAM magnetization against flip angle α (Fig. 1B), shows that signal loss is higher everywhere for the STEAM sequence, but particularly magnified for flip angles α which are moderately off-target, such as the approximately $\pi/4$ rad (45°) flip angle at (2). This translates to a severely amplified signal losses in STEAM in moderately under-flipped regions in the sample (e.g. (2) in Fig. 1A). It also leads to smaller spatial extent of high signal spots (e.g. (1) in Fig. 1A) and larger extent of low signal or drop-out spots (e.g. (3) in Fig. 1A). This demonstrates the increased need for achieving B_1+ homogeneity for whole brain STEAM imaging at UHF.

To this end, we introduce the k_T-dSTEAM sequence which is capable of acquiring diffusion-weighted images with improved signal homogeneity in the three pulse STEAM sequence, for whole human brain post mortem imaging.

This proposed sequence (Fig. 2C) employs composite k_T-points RF pulses, in contrast to the standard dSTEAM (Fig. 2A) with simple non-selective rectangular pulses. The resulting B_1+ profile is improved, which is manifested in a greatly homogenized STEAM signal over the specimen (Fig. 2C, right). For illustration and comparison, merely replacing only the excitation pulse with a composite k_T-points pulse, does not achieve the desired signal homogeneity (Fig. 2B).

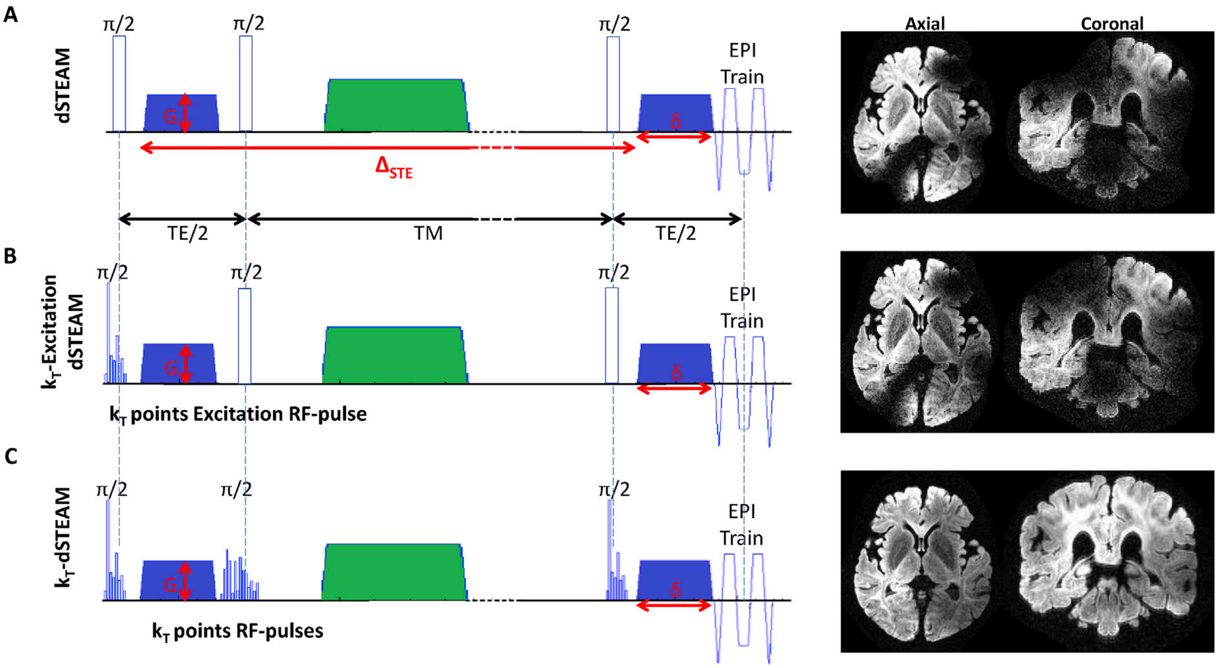

Fig. 2. Standard dSTEAM vs. k_T-dSTEAM sequence for whole brain imaging at 9.4T. (A) A standard dSTEAM sequence diagram with rectangular non-selective pulses, diffusion gradients (blue), spoiling gradient with enough momentum to dephase totally the SE signal (green) and the resulting image (right). Signal drop-out as a consequence of B_1^+ inhomogeneities is clearly visible. (B) For comparison, a dSTEAM sequence where only the excitation pulse was replaced with an optimized composite k_T-points pulse. This replacement does not improve signal homogeneity sufficiently. (C) The proposed k_T-dSTEAM sequence, in which all rectangular pulses are replaced with optimized composite k_T-points pulses, with greatly reduced local signal loss. TE: echo time, TM: mixing time, Δ_{STE}: stimulated echo diffusion time, G: diffusion gradient amplitude, δ: diffusion gradient duration.

2.2. k_T-dSTEAM signal model

A full 3D acquisition considerably improves SNR efficiency for whole brain ex vivo acquisitions (Miller et al., 2011), but also requires relatively short TRs close to T_1 values which means that the signal reaches a steady state condition. In the case of STEAM, the STE signal possesses an extra component which is dependent on T_1, as shown in (Alexander and Dyrby, 2013; Lundell et al., 2014). A proper steady state is achieved if the signal is completely spoiled before the action of the excitation pulse and the primary SE signal is also completely spoiled before the action of the recalling pulse. If those conditions are fulfilled, the STE signal equation can be adapted to:

$$S_{STE}(TR, TM, TE, \alpha_i) = \frac{1}{2}\left(1 - \exp\left(-\frac{TR - TM}{T_1}\right)\right)\sin(\alpha_1)\sin(\alpha_2) \sin(\alpha_3)\exp\left(-\frac{TM}{T_1}\right)\exp\left(-\frac{TE}{T_2}\right) \tag{2}$$

The diffusion-weighting of the resulting STE signal requires the use of diffusion gradients before the storing and after the recalling pulses (Fig. 2). The advantage compared to PGSE is to obtain high diffusion-weighting data at short TE's (Merboldt et al., 1991), since the diffusion time is extended with TM.

Proper consideration of the T_1 components in the signal decay, including the TR-TM steady-state term shown in equation (2), would allow for the analysis of diffusion-weighted data from a varying-TM multi-shell dSTEAM acquisition. Since the change in TM implies both a different diffusion-weighting and a different T_1 decay, the combined images can be analyzed if the effect of T_1 decay is incorporated into the diffusion equation:

$$dS_{STE}(TR, TM, TE, \alpha_i,\ b) = S_{STE}(TR, TM, TE, \alpha_i)\exp\left(-(\gamma G\delta)^2 \left(\Delta_{SE} + TM_i - \frac{\delta}{3}\right)D\right) \tag{3}$$

If the acquisition scheme for diffusion data only varies TM and all flip angles are considered to be appropriately homogenized and close to $\pi/2$ rad, then the equation is simplified to:

$$dS_{STE}(TM_i,\ b) = S_0^*\left(1 - \exp\left(-\frac{TR - TM_i}{T_1}\right)\right)\exp\left(-\frac{TM_i}{T_1}\right) \exp\left(-(\gamma G\delta)^2\left(\Delta_{SE} + TM_i - \frac{\delta}{3}\right)D\right), \tag{4}$$

where S_0* represents the T_1-unweighted signal (in the limit of TM = 0). However, this requires T_1 to be known, and it must be estimated prior to diffusion analysis, as described below. If all data are acquired at the same TM, the signal equation returns to a form similar to the one used for PGSE:

$$dS_{STE}(TM_0,\ b) = S_0\ \exp\left(-(\gamma G\delta)^2\left((\Delta_{SE} + TM_0) - \frac{\delta}{3}\right)D\right) \tag{5}$$

2.3. Ex vivo specimens and data acquisition

Two formalin-fixed whole brains (specimen 1 and specimen 2) and one formalin-fixed left hemisphere specimen (specimen 3), acquired from subjects without known neurological or psychiatric diseases, were used in this study. Specimen 1 was from a donor giving informed consent under the Maastricht University, Department of Anatomy and Embryology body donation program (post mortem interval to fixation: 12 h, fixation to scanning: 30 months) as regulated by the Dutch law for the use of human remains for scientific research and education ("Wet op de Lijkbezorging"). Specimen 2 was obtained from the University of Rostock body donor program (post mortem interval to fixation: 32 h, fixation to scanning: 25 months). Specimen 3 (post mortem interval to fixation: 3.5 h, fixation to scanning: 3 months) was borrowed from Dr. R.N. Kooijmans (NIN/KNAW), and were originally obtained from The Netherlands Brain Bank (NHB1037 - 121/2018), Netherlands Institute for Neuroscience, Amsterdam (open access: www.brainbank.nl). All material has been collected from donors for or from whom a written informed consent for a brain autopsy and the use of the material and clinical information for research purposes had been obtained by the NBB. Each specimen was immersed in its fixation solution and then enclosed in a 3D conformal container printed using a watertight, chemically resistant material SOMOS XC11122 (DSM Heerlen) (Roebroeck et al., 2015). The specimen vary quite strongly in their white matter T_1, T_2 and diffusivity D parameters, as a consequence of their post mortem interval (PMI), fixation time and general tissue quality, discussed in more detail elsewhere (D'Arceuil and de Crespigny, 2007; Miller et al., 2012a; Roebroeck et al., 2018; Sun et al., 2005). Specimen 1 had a white matter T_1/T_2/D average of approximately $0.350\,s/0.009\,s/2.0 \times 10^{-4}\,mm^2/s$, which is relatively low for fixed ex vivo brain specimen. Specimen 2 and specimen 3 had a white matter T_1/T_2/D average of approximately $0.550\,s/0.018\,s/2.2 \times 10^{-4}\,mm^2/s$, which are relatively high for fixed ex vivo brain specimen. These differences, particularly in T_2 and D, served to investigate the performance of k_T-dSTEAM over a reasonably expected range of tissue quality.

The k_T-dSTEAM sequence was implemented on a 9.4T, 82 cm bore Siemens MAGNETOM research scanner (Siemens Healthineers, Erlangen, Germany) with maximum gradient amplitude of 80 mT/m and maximum slew rate of 330 mT/m/ms per physical axis. For RF transmission and reception, a custom-built 9.4T whole-brain coil (400 MHz) with 24 receive channels and 8 transmit channels was used (Roebroeck et al., 2015). In this coil, the 24 receive coil loops are laid out as a phased array, conformal and tightly fitting to the brain container, with on-coil preamplifier circuits and decoupled by geometric overlap and preamplifier decoupling. The eight separate transmit loops have a 2 × 2 x 2 layout, placed on 2 separate hemispheric formers (4 transmit channels in a 2 × 2 pattern on each half), allowing for full 3D parallel transmission.

The composite k_T-point pulses in k_T-dSTEAM are created analogous to the composite k_T-point excitation pulse in GRE sequences (Cloos et al., 2012; Tse et al., 2016). Each one is a globally non-selective composite pulse with 8–16 sub-pulses, optimized for B_1+ homogeneity (Fig. 2). For the k_T-points pulse design, a B_0 map (Cusack and Papadakis, 2002) and transmit RF profile (B_1+) map for each of the transmit channels were acquired with transmitting phase-encoded by using a T_2 and T_2* compensated version of DREAM (Nehrke and Bornert, 2012). B_0 shimming and k_T-point pulse calculation for B_1+ shimming was performed by the approach established in Setsompop et al. (2008) and Tse et al. (2016), using custom-written MATLAB routines (MathWorks, MA, USA). For the k_T-points pulses, the sub-pulse spacing was set to 180 μs for all three composite pulses. The excitation and recalling pulses used 8 sub-pulses, whereas the storing pulse was implemented with 16 composite sub-pulses as shown in Eggenschwiler et al. (2014) and Eggenschwiler et al. (2016).

After B_0 shimming and composite RF pulse calculations, k_T-dSTEAM images were acquired for T_1 and T_2 relaxometry, and diffusion analysis. The acquisition parameters per study are specified in Table 1. The imaging was performed using a segmented 3D EPI readout. All scans were acquired at the same field of view (FoV) of 162 × 150 mm2 in sagittal orientation, readout along the anterior-posterior (AP) direction (parallel to the scanner bore) with an EPI-factor of 5. All diffusion acquisitions used for modeling (for parameters see Table 1) were acquired with a minimum of 24 directions per shell and accompanied by 3 or 4 b_0-weighted volumes per shell. The crusher gradients around the storing and recalling pulses in these b_0 volumes accumulated an actual b-value approximately 200 s/mm^2, which we therefore also refer to as low b-value or low-b. In some of the acquisitions, a factor of two undersampling was applied along the partition encoding dimension (2x PA) in the left-right (LR) direction of the brain. In those cases, a low-resolution reference image (autocalibration signal or ACS image) was acquired using the same sequence and parameters but at 2 mm isotropic resolution and full encoding, for subsequent offline reconstruction in Matlab. Noise-only scans were also acquired in order to estimate the channel-by-channel noise covariance matrix (Kellman and McVeigh, 2005).

For the purpose of comparing varying-TM multi-shell acquisition to same-TM multi-shell acquisition we acquired, for specimen 3, a short-TM $b = 4000\ s/mm^2$ (b4k) shell and long-TM $b = 6000\ s/mm^2$ (b6k) shell and added a matched long-TM b4k shell. To show the achievable advantages of k_T-dSTEAM over PGSE in this study, a matched set of diffusion acquisitions at different b-values were acquired on the same specimen as specified in Table 1. For comparison purposes, the diffusion gradient amplitude (G) was set to the maximum possible (80 mT/m) for both sequences so that TE could be minimized. To avoid B_1+ inhomogeneity in the PGSE acquisitions, the k_T-dSTEAM was converted to k_T-PGSE accordingly, by changing the phase (from x to z) and flip angle (from $\pi/2$ to π rad) of the storing pulse and removing the recalling pulse. This allowed for the use of the same composite pulses to achieve the same level of B_1+ homogenization.

2.4. Image reconstruction, signal comparison and analysis

All the acquired images were reconstructed offline in MATLAB. EPI ghost correction (by odd-even echo offsets) were corrected using phase navigators (Pfeuffer et al., 2002) and Inverse Fourier transforms were applied without windowing along all axes. Accelerated undersampled relaxometry T_1w and T_2w data were reconstructed using ESPIRiT (Uecker et al., 2014) as implemented in the BART toolbox (Tamir et al., 2016), using the low-resolution reference image and the noise covariance matrix. For diffusion-weighted data, covariance-weighted root sum-of-squares (rCovSos) reconstruction (Kellman and McVeigh, 2005; Triantafyllou et al., 2011) was used for channel combination to achieve a superior SNR compared to unweighted root sum-of-squares (rSoS).

After offline image reconstruction, several analyses were performed. Signal-to-noise (SNR) comparisons between k_T-PGSE and k_T-dSTEAM were made for equal b-values ($4000\ s/mm^2$ and $6000\ s/mm^2$), as well as between k_T-dSTEAM volumes at different b-values and TM's ($4000\ s/mm^2$ at TM of 0.134 s, $4000\ s/mm^2$ at TM of 0.205 s and $6000\ s/mm^2$ at TM of 0.205 s). Image SNR values were calculated as mean(signal)/std.dev(noise) over spherical volumes of interest (VOIs), 9 voxels in diameter. The mean signal was estimated in different areas in specimen 3 and the noise standard deviation was obtained using 4 VOIs in signal-free image background regions.

All quantitative T_1 (qT_1) and T_2 (qT_2) and diffusion model fitting from the k_T-dSTEAM data were performed using the Microstructure Diffusion Toolkit (MDT, https://github.com/cbclab/MDT) by nonlinear GPU accelerated optimization (Harms et al., 2017). Powell optimization with Patience 20 was employed for qT_1 and qT_2 estimation using equation (2). Unweighted signal (S_0) in equation (2) was initialized using the highest measured signal (usually the lowest TE or TM) and an offset-Gaussian likelihood function was used to account for the Rician rectified noise floor. The noise level was estimated by selecting a region of interest (ROI) in the signal-free image background and calculating its complex standard deviation by assuming a Rayleigh distribution (Gudbjartsson and Patz, 1995).

Multi-shell k_T-dSTEAM data were analyzed both separately as single shells (of b4k and b6k), and jointly as multi-shell data using the same TM (same-TM, in specimen 3) and varying TM (varying-TM, in specimen 1 and 3). Single-shell data was analysed with Diffusion Tensor Imaging (DTI) and Ball&Stick (B&S) with one ($B\&S_{r1}$) and two ($B\&S_{r2}$) sticks models using equation (5). The diffusivity for the stick compartment was fixed to the mean diffusivity obtained from the corresponding DTI analysis. For same-TM multi-shell data, the analysis was identical to the one used for single-shell analysis (i.e. using equation (5)). The analysis for varying-TM multi-shell data was performed in a 5-step cascade approach summarised in Fig. 3. First, the qT_1 obtained from relaxometry fitting (step 1, Fig. 3) was used as a fixed T_1 value to disentangle the T_1 and diffusion contributions to the signal between shells using equation (4) (steps 2 to 4, Fig. 3). Finally, Diffusion models $B\&S_{r1}$ and $B\&S_{r2}$ were estimated with fixed S_0 and T_1 contributions (step 5, Fig. 3). Again, Powell optimization with patience 20 was employed for all the cases. After modeling, a voxel-wise model selection of the optimal number of stick orientations was performed ($B\&S_{r2}$ selected) by selecting voxelwise the model corresponding to the lowest Bayesian Information Criteria (BIC). In addition, if the stick fraction was lower than 10% (for $stick_0$) and 17.5% (for $stick_1$) during model optimization then the diffusivity is considered as null to help avoid multiplicity in the stick orientations.

As an illustration of the resolution effects on tractography, deterministic streamline tractography was performed on the DTI modeling results of the 1000 μm and 400 μm whole brain volumes (specimen 1 and specimen 2, respectively). Simple deterministic DTI tractography was chosen to highlight the effect of data resolution, rather than tractography algorithm sophistication. The tractography parameters used for both resolutions were: propagation direction by the truncated tensor

Table 1

k_T-dSTEAM relaxometry and diffusion acquisitions parameters and specimens used in this study. All acquisitions were performed using isotropic resolution. For diffusion, each b-value corresponds to a single mixing time (longer TMs for higher b-values). A sequence of timing parameters, such as TM or TE, are described as low:step:high. The acquisition time, on the other hand, is referred to as hrs:min:sec. Total acquisition times includes all volumes (for diffusion, including b_0 images). In the case of PGSE, the TM column reports the diffusion gradient duration (δ) and diffusion time (Δ) used per acquired b-value as indicated in the relevant PGSE cell. 2x PA: a factor of two undersampling was applied along the partition encoding (3D phase encoding) dimension.

Measurement (Specimen)	Resolution [μm] (Acquisition scheme)	TR [sec]	TE [sec]	TM [sec]	b-values [s/mm^2] (# directions)	Acquisition time (per volume/total)
T_1 relaxometry (Specimen 1)	1000 - EPI 5 – 2x PA	1.000	0.014	0.060 : 0.030 : 0.420	Not applicable	00:33:37/05:36:10
T_2 relaxometry (Specimen 1)	1000 - EPI 5 – 2x PA	0.350	0.014, 0.016 : 0.004 : 0.044	0.120	Not applicable	00:11:46/01:45:54
Diffusion (Specimen 1)	1000 - EPI 5	0.350	0.025	0.134, 0.205	2000 (1), 4000 (36), 6000 (48)	00:23:35/36:56:50
Diffusion (Specimen 1)	500 - EPI 5 – 2x PA	0.350	0.026	0.065, 0.135	2063 (24), 4034 (36)	00:53:49/60:05:43
Diffusion (Specimen 2)	1000 - EPI 5	0.350	0.025	0.065, 0.135	2000 (1), 4000 (1), 6000 (1), 8000 (1)	00:23:35/01:34:20
Diffusion (Specimen 2)	400 - EPI 5	0.350	0.027	0.096	3000 (20)	02:23:44/52:42:08
T_1 relaxometry (Specimen 3)	1000 - EPI 5	0.450	0.025	0.050, 0.120 : 0.060 : 0.360, 0.450	Not applicable	00:17:17/02:00:59
Diffusion (PGSE) (Specimen 3)	1000 - EPI 5	0.450	0.054, 0.061	(δ, Δ): (0.022, 0.025), (0.026, 0.029), (0.029, 0.031)	4059 (36), 6082 (1)	00:17:17/11:48:37
Diffusion (STEAM) (Specimen 3)	1000 - EPI 5	0.450	0.025	0.134, 0.205, 0.205	4059 (36), 4059 (36), 6085 (48)	00:17:17/38:18:41

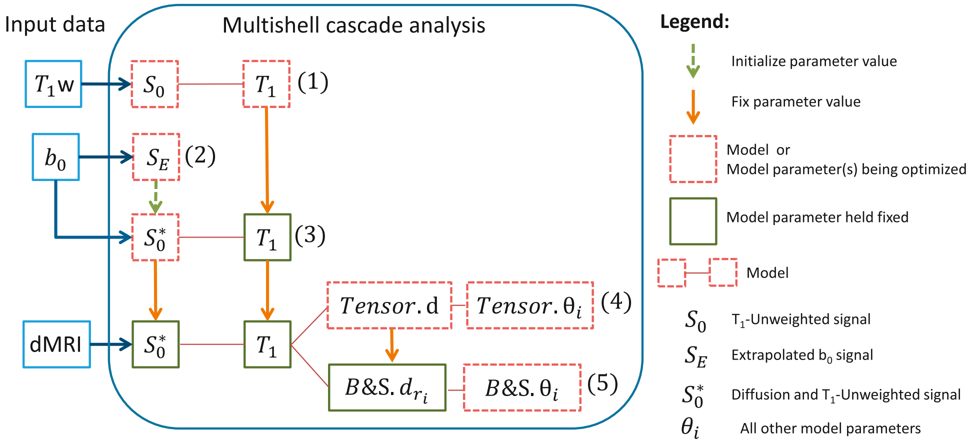

Fig. 3. k_T-dSTEAM cascade data analysis using nonlinear multi-shell diffusion model optimization. Parameters in more complex diffusion models are initialized with or held fixed at, values from simpler models (steps 4–5). Simpler models are estimated from separate T_1 relaxometry data (step 1) and the b_0 volumes (step 2 and 3).

projection operator (Roebroeck et al., 2008; Westin et al., 2002), trilinear interpolation, Euler integration, fractional anisotropy threshold of 0.1, step size of 0.4 mm and angle threshold of 35° leading to minimum radius of curvature of 0.5729 mm. Tractography was performed across the whole brain and seeded using a WM mask in a 5 × 5 x 5 grid per 1000 μm voxel and a 2 × 2 x 2 grid per 400 μm voxel to match seeding density.

To compare deterministic crossing fiber tractography in the cerebellar peduncle between the single-shell B&S$_{r2}$ model, multi-shell B&S$_{r1}$ model and multi-shell B&S$_{r2}$ model, the same tractography parameters were used in the 1000 μm resolution data of specimen 1, except for: propagation direction by selection of the most collinear local direction, 4th-order Runge-Kutta integration and angle threshold of 30°. Cerebellar peduncle tractography was seeded using a box mask in a 3 × 3 x 3 grid per 1000 μm voxel covering the cerebellar peduncle volume and exclusion masks were positioned 5 mm below and 5 mm above the seeding mask to exclude the cortico-spinal tract (CST) streamlines.

3. Results

The results are organised as follows. We first validate the predicted improvement of k_T-dSTEAM over more conventional PGSE dMRI in the large-sample-large-bore case, through a comparative study between (k_T)-PGSE and k_T-dSTEAM. Subsequently, we use the superior SNR efficiency of k_T-dSTEAM for ultra-high resolution whole brain diffusion MRI. We then show how this sequence can be conveniently used for quantitative T_1 and T_2 mapping, by relaxometry over varying TEs and TMs. This is a prerequisite for multi-shell diffusion acquisition and multi-orientation analysis, which we focus on in the final subsection.

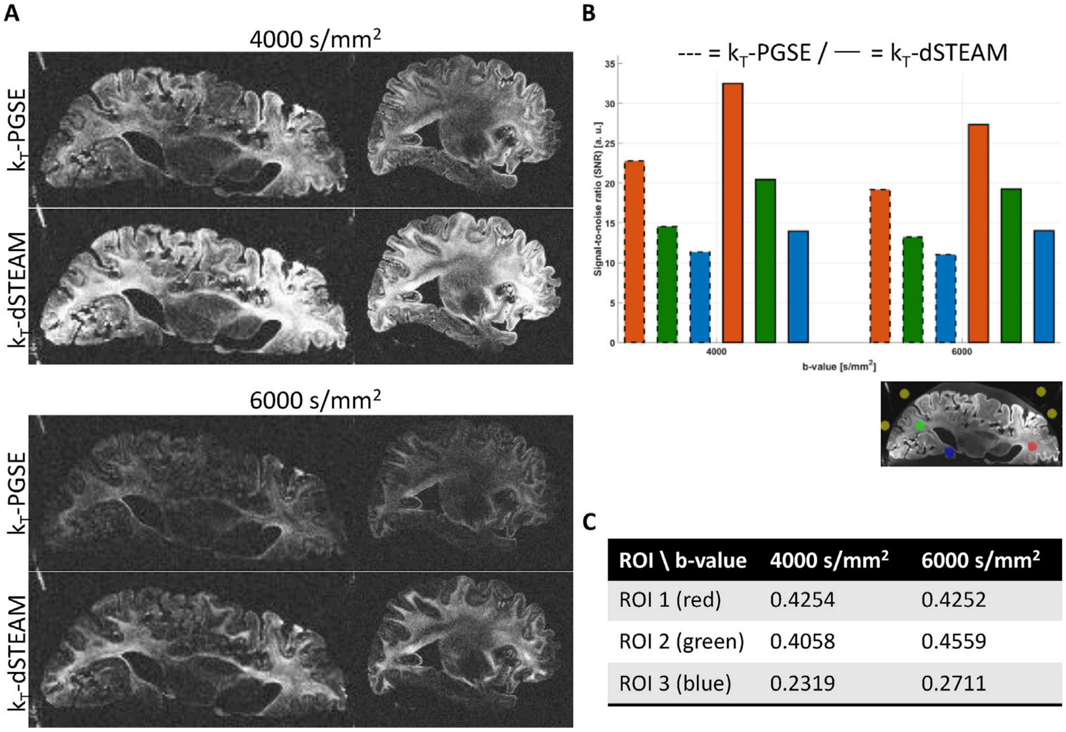

ROI \ b-value	4000 s/mm²	6000 s/mm²
ROI 1 (red)	0.4254	0.4252
ROI 2 (green)	0.4058	0.4559
ROI 3 (blue)	0.2319	0.2711

Fig. 4. k_T-dSTEAM and k_T-PGSE signal and SNR comparison. (A) Transverse (left) and sagittal (right) views for single diffusion weighted volumes of specimen 3 acquired at b-values of 4000 s/mm^2 (top) and 6000 s/mm^2 (bottom) for k_T-dSTEAM and k_T-PGSE, all with the same contrast scaling. (B) SNR in three different areas (red, green and blue ROIs in the figure inset, with image noise evaluated in the yellow ROIs) for both pulse sequences and both b-values. (C) The fractional differences between k_T-dSTEAM SNR and k_T-PGSE SNR for each ROI and b-value.

3.1. Comparative study between (k_T)-PGSE and k_T-dSTEAM

To compare the SNR efficiency of k_T-dSTEAM to that of a conventional PGSE acquisition, a matched set of diffusion acquisitions at different b-values were acquired on the same specimen. The same TR and maximum diffusion gradient amplitude was used with minimized TE (see Table 1). Furthermore, the same k_T-points B_1+ homogenization was used in the PGSE acquisitions, which we therefore refer to as k_T-PGSE. Fig. 4 shows the k_T-PGSE vs k_T-dSTEAM comparison for specimen 3 at b-values of 4000 and 6000 s/mm^2. For both b-values, k_T-dSTEAM images qualitatively show higher signal in comparison to k_T-PGSE (Fig. 4A). This is corroborated quantitatively by the estimated SNR in three different areas along the specimen (Fig. 4B). In the areas where the signal is high (red ROI) or moderately high (green ROI), the SNR for k_T-dSTEAM is over 40% higher than for k_T-PGSE, and over 20% higher in the low signal area (blue ROI). In ROI 2 and 3, but not ROI 1, the k_T-dSTEAM SNR improvement shows a tendency to increase from $b = 4000$ s/mm^2 to $b = 6000$ s/mm^2. Note that the SNRs reported here are for diffusion weighted single volumes (arguably the worst-case SNR), whereas in the literature the SNR for b_0 volumes is often reported (arguably the best-case SNR).

To assess the effects of SNR differences on dMRI analysis, Fig. 5 shows the mean b_0 (S_0, Fig. 5A) and fractional anisotropy (FA, Fig. 5B) parameter maps from DTI model fitting for the k_T-PGSE and k_T-dSTEAM data at the same b-value of $b = 4000$ s/mm^2 (b4k). The estimated S_0 for k_T-PGSE is lower along the entire specimen than the S_0 for k_T-dSTEAM, reflecting similar signal level differences as the diffusion-weighted volumes in Fig. 4. The FA maps show even clearer differences with lower and noisier FA estimates for k_T-PGSE, reflecting the known downward bias in FA estimates caused by low SNR (Jones and Basser (2004)).

3.2. Ultra-high resolution whole brain diffusion MRI

Fig. 6 shows single volumes of whole brain k_T-dSTEAM acquisitions for both the low-T_2 specimen 1 (Fig. 6A) and the high-T_2 specimen 2 (Fig. 6B) at two different b-values (low and high) and two resolutions (high and ultra-high). In the low-b acquisitions, the homogenous high-SNR STEAM signal can be appreciated, as well as the considerable increase in visible detail in going from the high (for whole brain diffusion acquisitions) resolution of 1000 μm isotropic to 8x (500 μm for specimen 1) or 16x (400 μm for specimen 2) higher isotropic resolution. The high b-value acquisitions (separately windowed and leveled) at 1000 μm isotropic show the effect of diffusion weighting using moderate b-values. At the much lower diffusivities in fixed post mortem tissue, the contrast achieved with these b-values is more subtle and dependent on the varying tissue diffusivity between samples. Notably, the WM contrast achieved with $b = 3000$ s/mm^2 in the high-T_2/high diffusivity specimen 2 is qualitatively higher than that achieved with $b = 4000$ s/mm^2 in the low-T_2/low diffusivity specimen 1. Finally, the high-b ultra-high resolution acquisitions show that the k_T-dSTEAM sequence is capable of producing imaging volumes in this extremely SNR-challenged regime, although there exists a clear trade-off in expending SNR towards higher diffusion weighting or higher resolution. Nevertheless, these images have sufficient SNR for diffusion imaging and tractography analysis.

Fig. 7 shows 400 μm single-shell results using DTI and B&S_{r1} models. The stick fraction map (Fig. 7A) displays good contrast between WM and GM, even in deep brain nuclei, as well as a tendency for a higher stick fraction in dense tracts such as the corpus callosum (CC) and CST. DTI primary eigenvectors (Fig. 7B) define both large WM tracts, such as CC, CST, and Cingulum (Cg), as well as radial directions in the GM at high spatial fidelity. The high resolution could potentially support tractography of the high curvature insertions (and exits) of white matter projections into (and out of) the cortex. Tractography at standard in vivo resolutions is known to be biased towards connecting gyral crowns, but not sulcal walls through white matter, which does not reflect known neuroanatomy (Van Essen et al., 2014).

Fig. 8 shows a comparison between tractography near the white/gray matter border in a gyral crown performed at high (1000 μm isotropic) and ultra-high (400 μm isotropic) resolutions. Using the same deterministic tractography parameters for both resolutions, streamlines can be

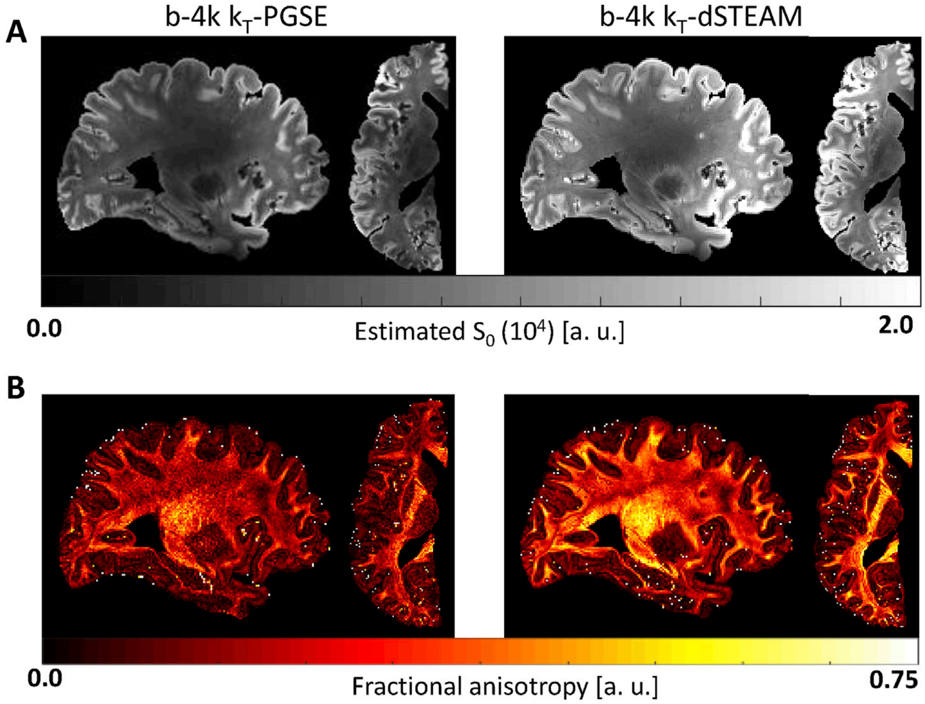

Fig. 5. k_T-dSTEAM and k_T-PGSE DTI analysis comparison. (A) Sagittal and transverse views for specimen 3 of the estimated mean b_0 (S_0) volume from DTI analysis performed at b-value of 4000 s/mm^2 for k_T-PGSE (left) and k_T-dSTEAM (right). (B) Sagittal and transverse views for the FA maps from DTI analysis for k_T-PGSE (left) and k_T-dSTEAM (right).

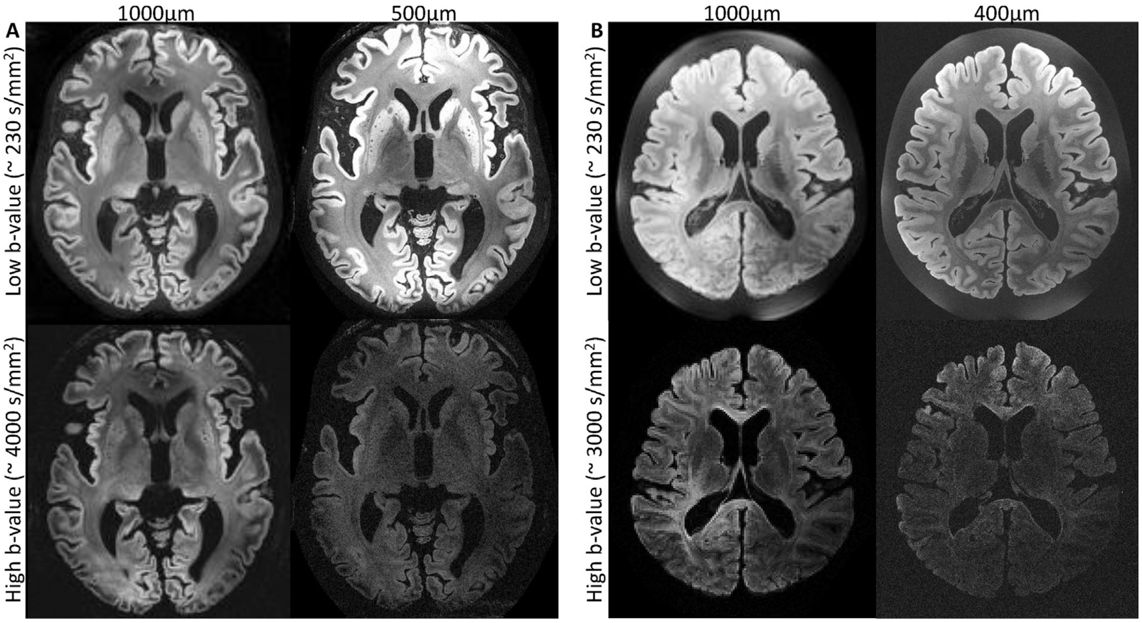

Fig. 6. Single diffusion direction volumes of k_T-dSTEAM whole brain acquisitions. (A) Mid-transverse views at high (1000 µm) and ultra-high (500 µm) resolution for specimen 1 for low (top) and high (bottom) b-values. (B) Mid-transverse views at high (1000 µm) and ultra-high (400 µm) resolution for specimen 2 for low (top) and high (bottom) b-values.

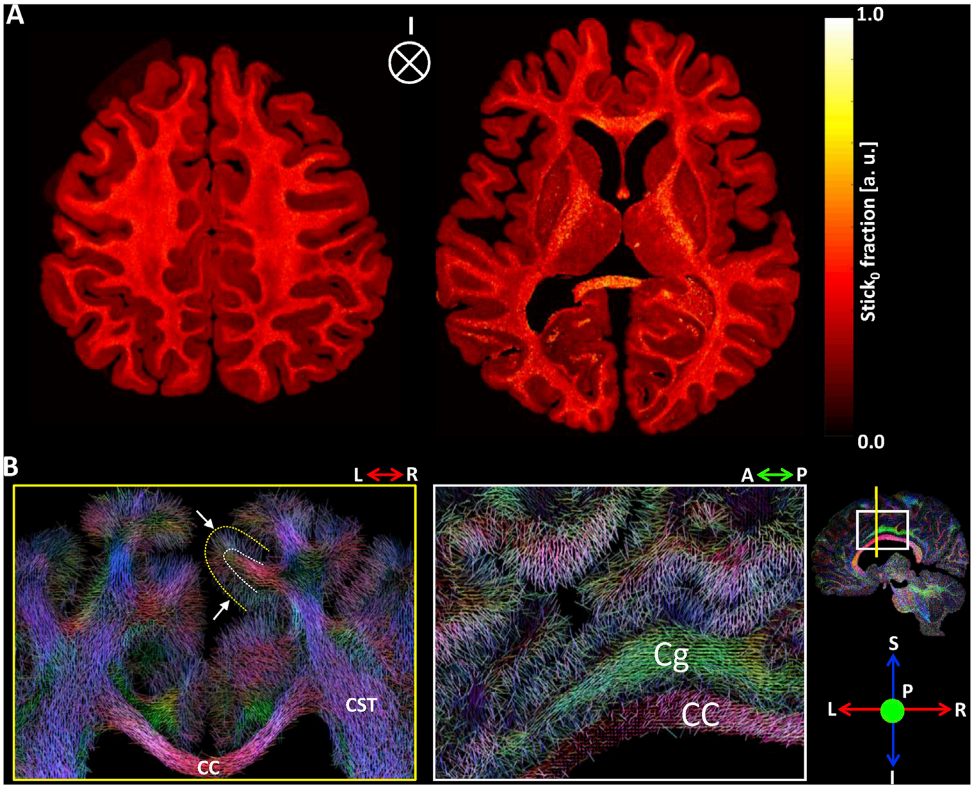

Fig. 7. k_T-dSTEAM single-shell 400 µm analysis results for specimen 2. A) Two axial slices through the Stick$_0$ fraction map resulting from a Ball&Stick$_{r1}$ model fit. B) Direction color coded DTI primary eigenvector in coronal (left) and sagittal (right) slices, the position indicated in the inset on the far right (and the direction color encoded in coronal view). Radial directions in the GM are indicated by the white arrows, between WM/GM boundary (dashed white line) and pial boundary (dashed yellow line). The primary eigenvector per voxel was elongated for visualization purposes and must not be confused with streamlines. CC: Corpus Callosum, Cg: Cingulum, CST: Cortico-Spinal Tract.

tracked beyond the WM/GM boundary. However, at the ultra-high resolution, the streamlines show less of the unwanted gyral crown bias, and more high-curvature paths connecting part of the sulcal wall through white matter.

3.3. *Relaxometry for quantitative T_1 and T_2 mapping*

STEAM sequence in general, and k_T-dSTEAM in particular, are highly suitable for both quantitative T_1 and T_2 mapping, by relaxometry on TM and TE respectively. Fig. 9 shows relaxometry data and corresponding quantitative T_1 (qT_1) and T_2 (qT_2) maps for specimen 1, estimated using equation (2). Fitted T_1 values were between about 0.3 and 0.7 s with no clear difference in qT_1 distribution between GM and WM, as is also clear from the visual lack of contrast in the qT_1 map (Fig. 9A). On the other hand, qT_2 values show a clear contrast between GM and WM, where the GM qT_2 values had a mode of 0.011 s and WM qT_2 values had a mode of

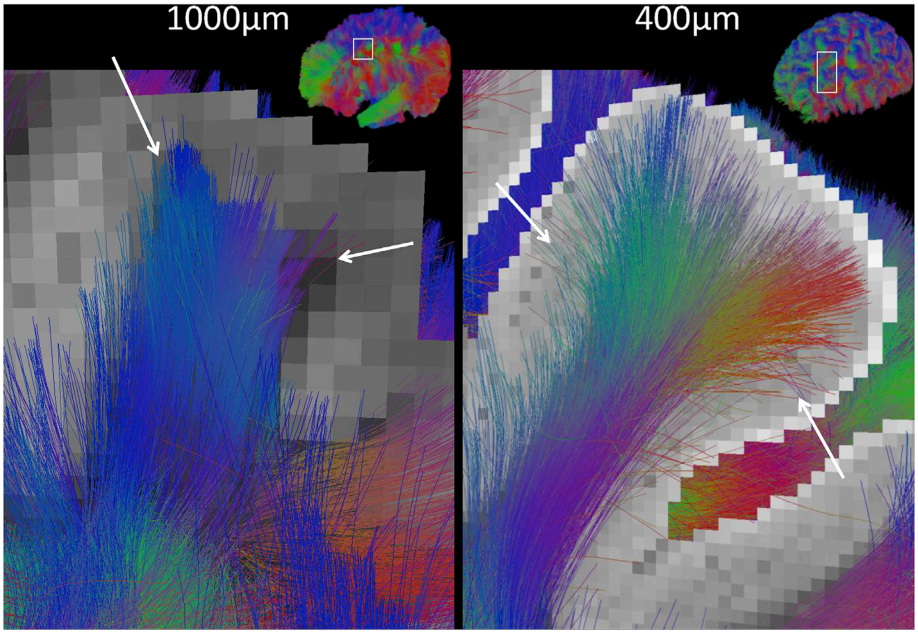

Fig. 8. k_T-dSTEAM diffusion tractography of the whole brain at high (1000 µm, left) and ultra-high (400 µm, right) resolution. Whole brain tractography is zoomed in to a gyral crown in frontal cortex indicated by the white box in the upper right inset. The arrows indicate, for both datasets, the approximate extreme extents of the gyral gray matter connectivity through white matter, which extends further into the sulcal wall at the higher resolution.

0.009 s, as indicated by the histograms in Fig. 9D. This agrees with the observations that little T_1 contrast remains between gray and white matter ex vivo and that, rather than T_2/T_2^* contrast, dominates the ex vivo image (Augustinack et al., 2014).

3.4. *Multi-shell diffusion acquisition and multi-orientation analysis*

Fig. 10 shows diffusion-weighted volumes acquired using k_T-dSTEAM at 1000 µm isotropic over a range of b-values in order to investigate the basic diffusion-induced signal decay and resulting image quality. High b-values could be achieved at reasonable SNR, up to 6000 s/mm^2 in the low-T_2/low-D specimen 1 (Fig. 10B) and up to 8000 s/mm^2 in the high-T_2/high-D in specimen 2. It is evident that for both specimens, SNR decreases as a function of b-value. At about $b = 4000$ s/mm^2, the higher unweighted signal but also higher diffusivity in GM compared to WM results in a loss of WM/GM contrast. For both specimens, the majority of diffusion-induced signal decay is observed between $b = 2000$ s/mm^2 and $b = 4000$ s/mm^2. It must be noted that the increased signal decay at higher b-values is not only intrinsic to the diffusion-weighting but it is also due to increasing T_1-weighting in the STE signal, since higher b-values are acquired with longer mixing times. Because T_1 for specimen 1 also is lower than that of specimen 2, this explains the lower CNR in specimen 1 at increasing b-value in comparison to specimen 2. However, the T_1-contribution in the signal decay doesn't affect the signal difference in different diffusion directions (Fig. 10B, bottom). In the case of specimen 1, where the mid-sagittal genu of the CC is taken as a reference, the signal decays faster along the LR (b_z) direction in comparison with perpendicular AP (b_x) or superior-inferior (SI – b_y) directions, as expected.

Having established the quality of k_T-dSTEAM data over multiple b-values, we analyzed both single-shell (using Equation (5)) and multi-shell k_T-dSTEAM data using the B&S$_{r2}$ model to investigate the support for the fitting of multiple fiber orientations in a voxel. Varying-TM multi-shell diffusion data analysis was performed using the qT_1 map (Fig. 9A) and Equation (4), following the pipeline shown in Fig. 3. The comparison between fitting results using single-shell and multi-shell analysis is shown in Fig. 11. Note that the S_0^* fit for the multi-shell analysis is an extrapolated fit of the 'zero-TM' non T_1-weighted signal derived from the b_0 volumes at the different TMs (Fig. 3), in contrast to the fits of S_0 in the single-shell cases. As expected, the magnitude of extrapolated S_0^* obtained in the multi-shell analysis is ~10 times higher than the b4k and b6k S_0 (the color scale is adjusted in Fig. 11 for the multi-shell S_0^*). The multi-shell S_0^* fit is more similar to the b4k S_0 fit than to the b6k S_0 fit, lacking the signal drop near the genu of the CC visible in the b6k S_0 fit (indicated with the white arrow). This is also reflected in the stick fraction and orientation maps: whereas the b6k single-shell analysis suffers from a rather noisy estimation at the frontal location, the multi-shell analysis achieves reasonable estimates everywhere. Although the stick fraction resulting from the multi-shell fit is well defined, it has a slightly elevated level compared to the single-shell fractions. This is quantified in Fig. 11B, where the linear regression through scatter plots shows higher stick fraction values for the multi-shell analysis, leading to lower than unity regression slopes α. This effect is stronger for b6k single-shell analysis ($\alpha = 0.6941$) than for b4k single-shell analysis ($\alpha = 0.8409$). However, the level differences in the stick fraction parameters do not seem to affect the orientation estimation, as shown in Fig. 11A (bottom) and C. Comparing Stick$_0$ orientations in clearly defined tracts, such as the splenium and genu of the CC and the optical radiations (see yellow mask in Fig. 11C), 60% of the orientations are within 10° and 80% of the orientations are within about 20°.

Next, we investigated the relative advantages of a varying-TM multi-shell acquisition and a same-TM multi-shell acquisition. To this end we acquired, for specimen 3, a short-TM b4k shell and long-TM b6k shell, as before, and added a matched long-TM b4k shell. As illustrated in Supplementary Fig. 1, there is a 10–15% decrease in SNR in going from the short-TM to the long-TM at b4k. However, this is relatively modest compared to the 25–30% SNR decrease in going from short-TM b4k to long-TM b6k. Therefore, it may be justified in some cases to forego the SNR advantage (in the b4k shell) of a varying-TM multi-shell acquisition and instead choose a same-TM multi-shell acquisition. Ball & Stick modeling (B&S$_{r2}$) of both the varying-TM and same-TM options on the same specimen shows that a high correlation in stick fraction ($R^2 = 0.926$) and highly similar fiber orientation fits are obtained, with 90% of single-tract orientations within 20° (Supplementary Fig. 2).

Fig. 12 shows the comparison between single orientation and multiple orientation analysis of k_T-dSTEAM multi-shell data and the resulting

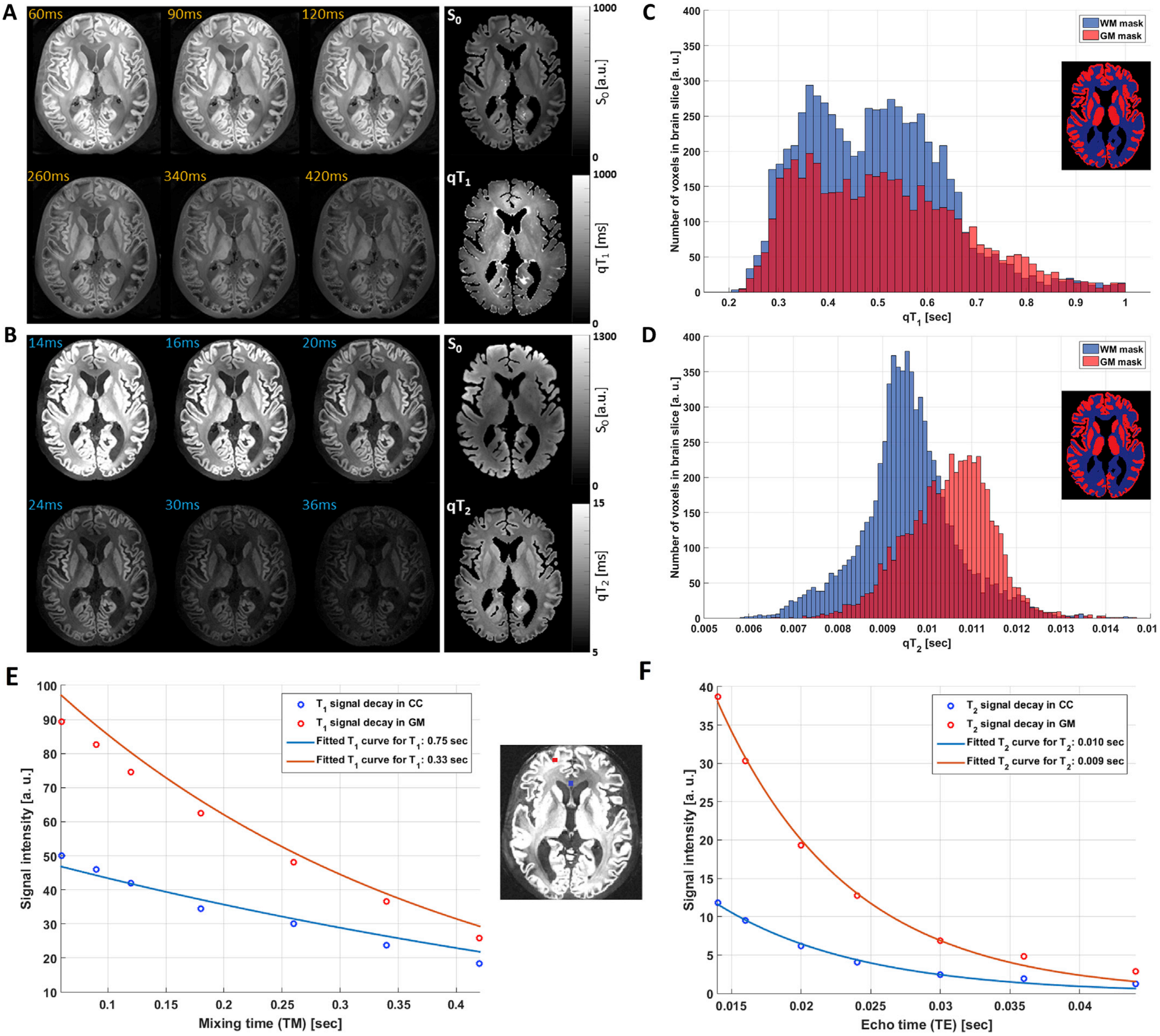

Fig. 9. k_T-dSTEAM relaxometry data and corresponding quantitative T_1 (qT_1) and T_2 (qT_2) maps for specimen 1. (A) Volumes at increasing mixing times showing T_1 signal decay (left), the corresponding qT_1 map from model fitting (middle), and (C) histograms of T_1 values along the slice separately for GM and WM masks. (B) Volumes at increasing echo times showing T_2 signal decay (left), the corresponding qT_2 maps from model fitting (middle), and (D) histograms of T_2 values along the slice separately for GM and WM masks. In contrast to the qT_1 histograms, qT_2 shows two peaks corresponding to WM and GM structures. (E) and (F) show the experimental T_1 and T_2 signal decay (circles) for the corpus callosum (CC, blue) and GM (red) and their corresponding T_1 and T_2 signal fitting (solid lines) respectively.

tractography in the cerebellar peduncle. The use of multi-shell multi-orientation tractography enables superior definition of crossing fiber structures, such as the raphe nuclei fibers (at the white arrow) and transverse pontine fibers (at the yellow arrow). This is true both in comparison to a multi-orientation analysis of the high-b single-shell data (Fig. 12A and B) and in comparison to the single orientation analysis of the multi-shell data (Fig. 12C and D).

4. Discussion

We show that k_T-dSTEAM achieves homogeneous T_1, T_2 and diffusion-weighted STEAM signal across human whole-brain and hemisphere specimens at 9.4T, solving a complex B_1+ homogenization problem for the three-pulse STEAM situation (Fig. 1) where current solutions do not suffice. As shown in Fig. 2B, the use of a composite k_T-points pulse only for excitation, as performed in a single pulse sequence such as GRE, is not enough to improve the signal homogeneity. k_T-dSTEAM's full application of composite pulses in all the three STEAM pulses is the only way to achieve B_1+ homogeneity (Fig. 2C). Composite k_T-points pulses have been used in sequences with more than one pulse before, as for example in TSE sequences (Eggenschwiler et al., 2014) but, to our knowledge, this is the first time they are used in a three pulse combination as is the case for STEAM.

Solving the challenge of getting a more homogeneous signal over intact human brains allowed us to use the advantages of STEAM diffusion weighting at UHF: creating a large part of diffusion contrast during T_1 decay, which is more advantageous at higher fields for fixed post mortem tissue. Even though a stimulated echo has half the signal (before T_1 or T_2 decay) of a spin echo from PGSE, in the whole ex vivo brain context of short T_2's, high b-values and low gradient performance, this is

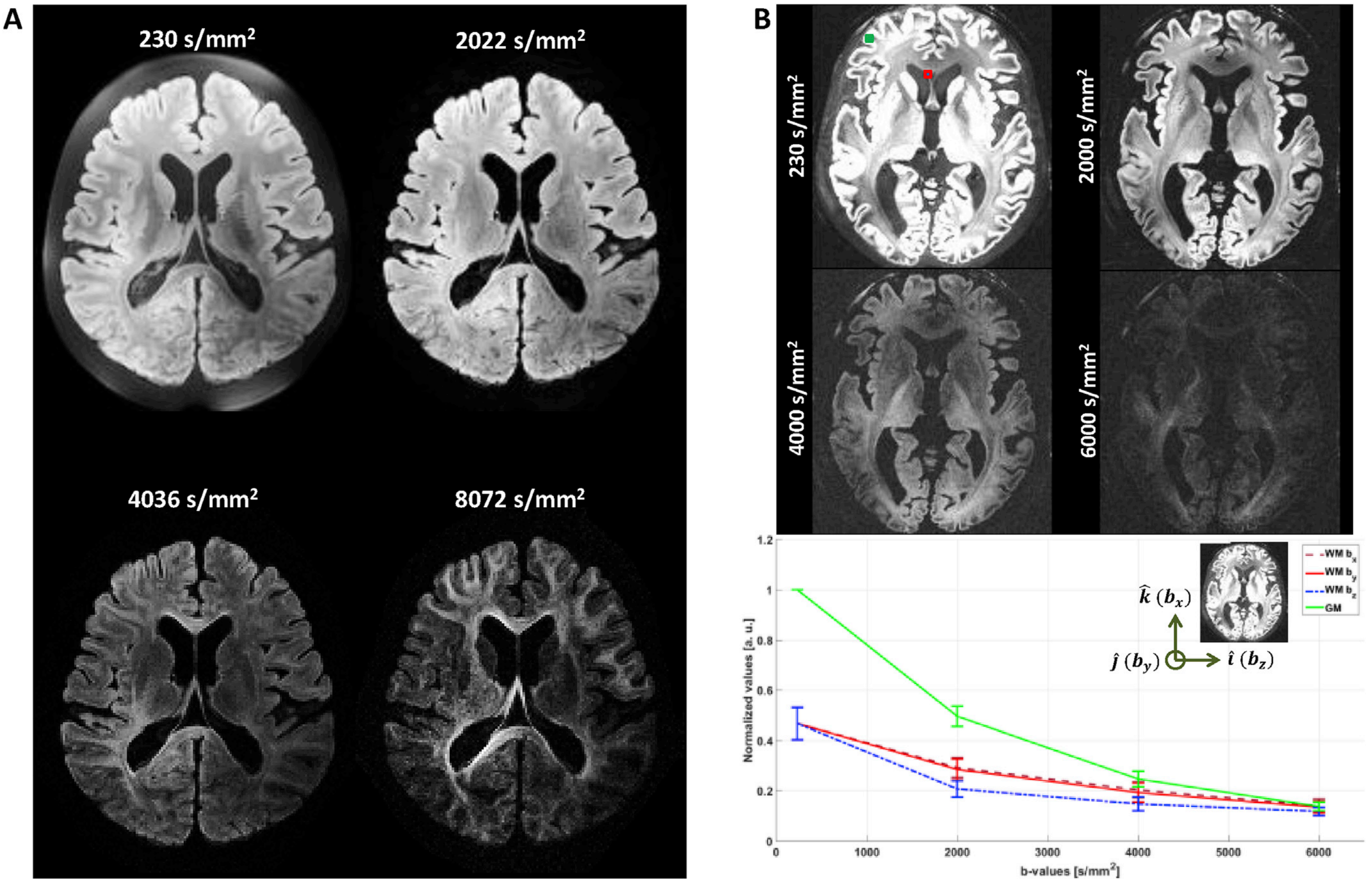

Fig. 10. k_T-dSTEAM diffusion-weighted data from low to high b-values for high-T_2/low-D specimen 1 (A) and low-T_2/low-D specimen 2 (B). Bottom in (B): Signal decay is shown in WM (in red and blue) and GM (in green) voxels (location indicated in the low-b image above) over b-values. For GM the direction is along AP (b_x), for WM the signal was plotted along the three perpendicular directions (red and magenta for AP (b_x) and SI (b_y) direction, and blue for LR (b_z) direction). Scanner coordinates ($\hat{i}$ – LR, $\hat{j}$ – SI, $\hat{k}$ – AP) and corresponding b-vector (b_z, b_y, b_x respectively) are indicated.

compensated with the advantage of less T_2 decay for a given b-value. This advantage is clearly illustrated in the k_T-PGSE vs. k_T-dSTEAM comparison (Figs. 4 and 5), showing a 20–40% SNR advantage for single diffusion weighted volumes for b-values of 4000–6000 s/mm^2, resulting in increased precision (reduced noise and variability) and accuracy (reduced bias) in dMRI modelling results. Of course, this does not conclude that high precision and high accuracy results could not be obtained with PGSE in the investigation of large human brain specimen. For instance, approximately 40% of SNR could be regained by doubling PGSE acquisition time and obtaining two averages of each volume. However, the fundamentally higher SNR-per-unit-time or SNR-efficiency of k_T-dSTEAM implies that k_T-dSTEAM could, in the same time, either boost SNR further by another 40% through averaging, or acquire twice the number of diffusion directions at the same SNR, making it a superior option. It should be noted that this conclusion is specific to the investigated case of human whole brain or hemisphere samples which are formalin-fixed and investigated in large-bore scanners. Small tissue samples can be investigated in smaller bore systems with much higher performing gradients, often in excess of 5 times the maximum gradient amplitude (80 mT/m) available in this study. In the small-bore high max-G situation, T_2 signal decay can be effectively mitigated by using very short gradient pulses and TEs, and high quality dMRI data can still be obtained for high b-values. However, in general, with higher field-strengths (and, hence, shorter T_2's), lower gradient performance, and higher desired b-values and diffusion times, the advantages of STEAM compared to PGSE will increase. Finally, whole human brain ex vivo diffusion MRI also could be achieved by in-situ acquisition very soon after death, at which point relaxation parameters, such as T_2 would be much closer to in vivo values. However, autolysis and tissue degeneration sets in almost immediately after death and progresses steadily in the hours thereafter. This means an in-situ ex vivo acquisition does not take place in a physiological steady-state condition. Moreover, acquisitions over several days, as performed for fixed brain samples, are therefore much more difficult.

In the future, further advantages can be achieved by utilizing the fact that the storing pulse splits the magnetization, where half the signal forms the first spin echo after the storing pulse and another half of the signal is stored along the longitudinal axis and is available for a stimulated echo. Both the SE and STE can be phase encoded and read out without interference (Frahm et al., 1985; Lutti et al., 2012), doubling the effective data rate. In the context of k_T-dSTEAM (Fig. 2), this would mean moving the spoiler gradient (green in Fig. 2C) towards the recalling pulse and adding a diffusion gradient and EPI train after the storing pulse, similar to those after the recalling pulse. One would then have both a diffusion-weighted SE and a diffusion-weighted STE signal available in the same acquisition time, although the b-value for the SE would always be considerably lower than that the STE. The practical use of both echoes in the same model fit necessitates further advances in modeling (including dealing with different diffusion- and T_1-weighted echo's, along the lines set out in this work for STE only) and careful consideration of the steady state conditions for the SE with corresponding spoiling and diffusion-gradient requirements.

4.1. Ultra-high resolution whole brain diffusion MRI

We use the k_T-dSTEAM sequence to obtain high resolution diffusion-

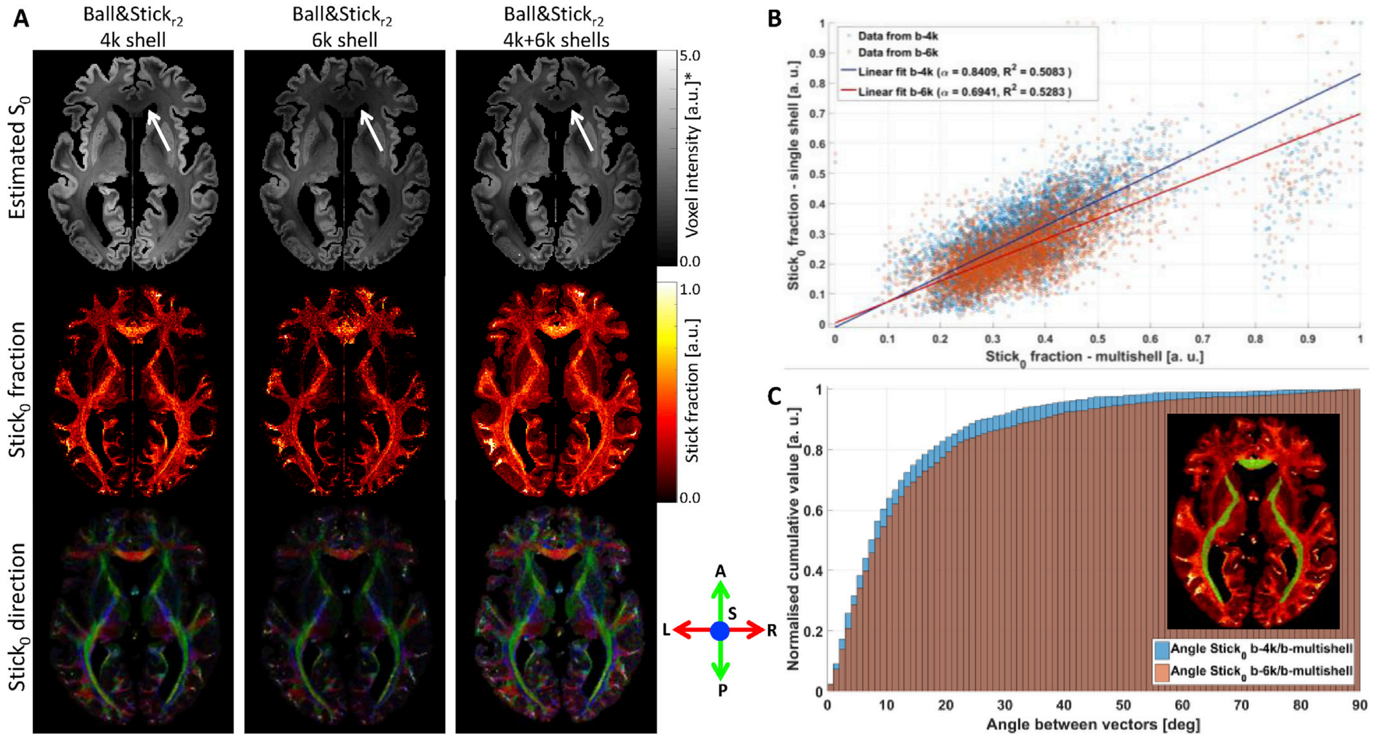

Fig. 11. Single-shell and multi-shell varying-TM k_T-dSTEAM diffusion analysis. (A) Comparison between single-shell (for the b4k shell, left, and the b6k shell, middle) and T_1-compensated multi-shell (b4k and b6k shell together, right) $B\&S_{r2}$ model fitting. Depicted is a transverse slice through the fitted S_0, the fraction of the first stick compartment $Stick_0$, and the color-coded direction of the first stick. (B) Correlation scatterplot between $stick_0$ fraction estimated using single shells (b4k in blue and b6k in orange) and multi-shell data with the corresponding linear regression with resulting slope/R^2 of 0.8409/0.5083 and 0.6941/0.5283 respectively. (C) Cumulative distribution histogram of the calculated angles between $stick_0$ vector obtained from single shells (b4k in blue and b6k in orange) and $stick_0$ estimated using multi-shell data for the voxels in the yellow mask in the inset. (*) Fitted unweighted signal (S_0*) for the multi-shell analysis results is 10 times greater than the unweighted signal from single-shell analysis.

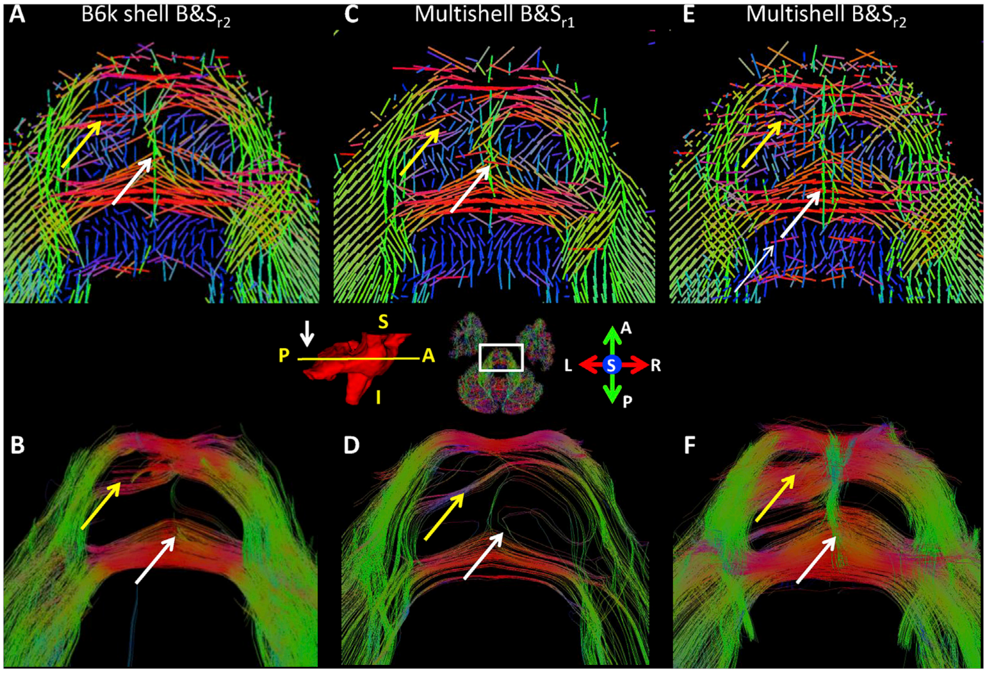

Fig. 12. k_T-dSTEAM multi-shell multi-orientation fitting and tractography of the cerebellar peduncle. A, C and E show the orientations of sticks using: the $B\&S_{r2}$ model for a single b6k shell (A), the $B\&S_{r1}$ model for multi-shell (b4k + b6k) data (C) the $B\&S_{r2}$ model for multi-shell (b4k + b6k) data (E) at the position indicated in the inset. B, D and F show the corresponding tractography on the orientations in A, C and E, respectively. Arrows indicate the raphe nuclei projections (green streamlines at the white arrow) and transverse pontine fibers (red streamlines at the yellow arrow).

weighted data in ex vivo specimens. We achieve ultra-high isotropic resolution whole brain dMRI data, 400 μm for high T_2/high-D specimen 2, which to our knowledge is the highest isotropic resolution reported for ex vivo whole brain diffusion acquisition. There exists a clear trade-off in higher diffusion weighting against higher resolution (at the same SNR). k_T-dSTEAM acquisitions at very high b-values (over 5000 s/mm^2) can be achieved in low T_2/low-D ex vivo samples and even higher b-values (over 8000 s/mm^2) in high T_2/high-D samples (Fig. 10) at 1000 μm isotropic.

Volumes with an 8x higher (500 μm), and even 16x higher (400 μm) resolution could be acquired at lower b-values (3000–4000 s/mm^2) as shown in Fig. 6. These ultra-high resolution acquisitions (400–500 μm) were calibrated to have enough SNR to be submitted to diffusion imaging and tractography pipelines (Figs. 7 and 8) and show that the k_T-dSTEAM sequence has enough SNR efficiency to produce useful data in this SNR challenged regime. It should be noted that the achievable resolution (at a given SNR and b-values) or the achievable b-value (at a given SNR and resolution) also depends on the quality of the sample, notably its T_2 value. Post-mortem acquisitions, in particular on large human samples which are scarce, need to be individually tailored to the quality of the sample, which explains our choices for differences in acquisitions, e.g. a ~2x higher resolution for specimen 2 (400 μm with a T_2 of 18 ms) than for specimen 1 (500 μm with a T_2 of 9 ms). As an illustration of the advantages of the higher resolution, tractography across the WM/GM border shows less of the unwanted gyral crown bias, and more high-curvature paths connecting the sulcal wall. Simple deterministic streamlining tractography was used to emphasize the effect of data resolution, rather than the effect of tractography technique. More sophisticated tractography could support high-curvature paths into the sulcal wall in lower resolution data, possibly with additional assumptions on likely insertion paths. Future combination of sophisticated tractography and the ultra-high resolution whole brain diffusion MRI data presented here could improve the fidelity of MRI-based human cortico-cortical connectomes.

4.2. *Relaxometry for quantitative T_1 and T_2 mapping*

Quantitative T_1 and T_2 could be estimated by using T_1w and T_2w k_T-dSTEAM acquisitions by varying TM and TE respectively. In the case of the qT_1 relaxometry, equation (2) can be used in short TR conditions. This short-TR equation is also used in the multi-shell diffusion analysis pipeline. The estimated S_0* in qT_1 relaxometry contains information about the proton density, coil sensitivity and T_2 with high contrast between WM and GM in S_0* maps. The resulting qT_1 values for WM and GM are approximately in a range between 0.2 and 0.7 s with no clear contrast between WM and GM. In contrast with the qT_1 estimation, the qT_2 map and corresponding histogram show a well-defined contrast between WM and GM structures in the specimen. The estimated S_0 for qT_2 modelling shows little contrast between WM and GM, containing information about the proton density, coil sensitivity, and T_1. This is in agreement with observations that T_2/T_2*, rather than T_1, dominates the contrast in ex vivo images (Augustinack et al., 2014).

4.3. *Multi-shell diffusion acquisition and multi-orientation analysis*

Multi-shell analysis of k_T-dSTEAM at variable TM (varying-TM) is shown as an approach for ex vivo data analysis which is adapted to the strengths of STEAM diffusion weighting. The varying-TM analysis incorporates qT_1 parameter maps and uses the cascaded modeling pipeline in Fig. 3, which is based on the signal model in equation (4). This allows parameter estimates, such as stick volume fractions and orientations, for varying-TM data which are not well suited for analysis with standard models. The advantage of acquiring varying-TM data is that SNR at each shell is maximized, rather than compromising SNR for lower b shells (c.f Supplementary Fig. 1). Therefore, the high SNR of low b shells and the high orientation contrast of high b shells are used effectively. Here, we used this gain for multi-orientation modeling and crossing-fiber tractography. An additional advantage of varying-TM multi-shell acquisitions is that they could support sophisticated diffusion microstructure modeling (Alexander et al., 2019) which relies on data with a range of different diffusion times, such as axon diameter modeling (Alexander et al., 2010; Assaf et al., 2008; Barazany et al., 2009; De Santis et al., 2016; Dyrby et al., 2012; Zhang et al., 2011). However, future varying-TM microstructure modeling would have to take the decreasing ADC with increasing diffusion time into account (De Santis et al., 2016; Jespersen et al., 2017; Kleinnijenhuis et al., 2018), as well as the microstructural changes due to autolysis after death (Dyrby et al., 2011, 2018; Roebroeck et al., 2018). Equation (4) currently does not contain TM-dependent ADCs, which may explain the constant slope difference between stick fractions estimated from the single-shell and varying-TM multi-shell data (c.f. Fig. 11B). It is important to note that the orientation modelling, which is the focus here, is not affected by any ADC weighting in the stick fraction as clearly shown in Fig. 12. The use of varying-TM multi-shell analysis is well suited for multi-orientation models as $B\&S_{r2}$ and $B\&S_{r3}$ since it enables the incorporation of high SNR dMRI volumes at different diffusion directions and at different b-values. This supports better modelling of crossing fibers such as in the brain stem (Fig. 12), by effectively using both low b shells and high b shells at the highest possible SNR and contrast. Future applications which aim at diffusion microstructure modelling of multi-shell data without the need for varying diffusion times, could employ the same-TM multi-shell acquisition (cf. Supplementary Fig. 2) without potentially introducing bias due to the varying-TM.

4.4. *Outlook*

In this work, k_T-dSTEAM data was acquired at 400–500 μm resolution with moderate 3000–4000 s/mm^2 b-values single-shell and at 1000 μm resolution with high 6000–8000 s/mm^2 b-values. A combination of ultra-high resolution and high b-values in the same dataset would have the combined advantage for tractography of delineating both high curvature fibers (by high resolution) and crossing fibers (by multi-shell multi-orientation modelling). However, under the current conditions, this would tax the SNR in the resulting data (or the acquisition times) too much. Nevertheless, such data could be acquired in the future by combining k_T-dSTEAM with one or more additional techniques. On the acquisition side, k-space undersampled acquisitions with parallel imaging reconstruction, as used in the relaxometry data here, can help balance the tradeoff between a number of diffusion direction volumes, amount of time per volume and SNR. Denoising approaches that use the redundancy present in many diffusion volumes can help in regaining SNR in SNR-starved acquisitions (Becker et al., 2014; St-Jean et al., 2016; Veraart et al., 2016). Finally, it has been shown that high-resolution/low-b data and low-resolution/high b data in the same specimen can be combined in the analysis to provide the advantage of both (Fan et al., 2017; Sotiropoulos et al., 2013). Such ultra-high resolution and multi-shell k_T-dSTEAM data have the potential to improve the fidelity of MRI-based human cortico-cortical connectomes.

Declaration of interest

None.

Acknowledgment

We thank Andreas Herrler for carefully selecting and fixing specimen 1 and making it available for this study. We also thank Katrin Amunts, Svenja Caspers and Karl Zilles for carefully selecting and fixing specimen 2 and making it available for this study. We also thank Roxana Kooijmans for carefully selecting and fixing specimen 3 and making it available for this study. AR and FJ were supported by an ERC Starting Grant (MULTICONNECT, #639938). AR was further supported by a Dutch science foundation (NWO) VIDI Grant (#14637). BP is partially funded by NWO VIDI Grant 016.Vidi.178.052 and NIH Brain Initiative (R01 MH111444; PI Feinberg).

Appendix A. Supplementary data

Supplementary data to this article can be found online at https://doi.org/10.1016/j.neuroimage.2019.116087.

References

Aggarwal, M., Nauen, D.W., Troncoso, J.C., Mori, S., 2015. Probing region-specific microstructure of human cortical areas using high angular and spatial resolution diffusion MRI. Neuroimage 105, 198–207.

Aggarwal, M., Zhang, J.Y., Pletnikova, O., Crain, B., Troncoso, J., Mori, S., 2013. Feasibility of creating a high-resolution 3D diffusion tensor imaging based atlas of the human brainstem: a case study at 11.7 T. Neuroimage 74, 117–127.

Alexander, D.C., Dyrby, T.B., Nilsson, M., Zhang, H., 2019. Imaging brain microstructure with diffusion MRI: practicality and applications. NMR Biomed. 32 (4), 3841.

Alexander, D.C., Hubbard, P.L., Hall, M.G., Moore, E.A., Ptito, M., Parker, G.J., Dyrby, T.B., 2010. Orientationally invariant indices of axon diameter and density from diffusion MRI. Neuroimage 52, 1374–1389.

Alexander, D.C., Dyrby, T.B., 2013. Diffusion Imaging with Stimulated Echoes: Signal Models and Experiment Design.

Assaf, Y., Blumenfeld-Katzir, T., Yovel, Y., Basser, P.J., 2008. AxCaliber: a method for measuring axon diameter distribution from diffusion MRI. Magn. Reson. Med. 59, 1347–1354.

Augustinack, J.C., Magnain, C., Reuter, M., van der Kouwe, A.J., Boas, D., Fischl, B., 2014. MRI parcellation of ex vivo medial temporal lobe. Neuroimage 93 Pt 2, 252–259.

Barazany, D., Basser, P.J., Assaf, Y., 2009. In vivo measurement of axon diameter distribution in the corpus callosum of rat brain. Brain 132, 1210–1220.

Bastiani, M., Oros-Peusquens, A.-M., Seehaus, A., Brenner, D., Moellenhoff, K., Celik, A., Felder, J., Bratzke, H., Shah, N., Galuske, R., Goebel, R., Roebroeck, A., 2016. Automatic segmentation of human cortical layer-complexes and architectural areas using diffusion MRI and its validation. Front. Neurosci. 10.

Becker, S.M., Tabelow, K., Mohammadi, S., Weiskopf, N., Polzehl, J., 2014. Adaptive smoothing of multi-shell diffusion weighted magnetic resonance data by msPOAS. Neuroimage 95, 90–105.

Bernstein, M.A., King, K.F., Zhou, X.J., 2004. Chapter 10 - correction gradients. In: Handbook of MRI Pulse Sequences. Academic Press, Burlington, pp. 292–362.

Buxton, R.B., 1993. The diffusion sensitivity of fast steady-state free precession imaging. Magn. Reson. Med. 29, 235–243.

Calabrese, E., Hickey, P., Hulette, C., Zhang, J., Parente, B., Lad, S.P., Johnson, G.A., 2015. Postmortem diffusion MRI of the human brainstem and thalamus for deep brain stimulator electrode localization. Hum. Brain Mapp. 36, 3167–3178.

Cloos, M.A., Boulant, N., Luong, M., Ferrand, G., Giacomini, E., Le Bihan, D., Amadon, A., 2012. kT -points: short three-dimensional tailored RF pulses for flip-angle homogenization over an extended volume. Magn. Reson. Med. 67, 72–80.

Cusack, R., Papadakis, N., 2002. New robust 3-D phase unwrapping algorithms: application to magnetic field mapping and undistorting echoplanar images. Neuroimage 16, 754–764.

D'Arceuil, H., de Crespigny, A., 2007. The effects of brain tissue decomposition on diffusion tensor imaging and tractography. Neuroimage 36, 64–68.

D'Arceuil, H.E., Westmoreland, S., de Crespigny, A.J., 2007. An approach to high resolution diffusion tensor imaging in fixed primate brain. Neuroimage 35, 553–565.

De Santis, S., Jones, D.K., Roebroeck, A., 2016. Including diffusion time dependence in the extra-axonal space improves in vivo estimates of axonal diameter and density in human white matter. Neuroimage 130, 91–103.

Dell'Acqua, F., Bodi, I., Slater, D., Catani, M., Modo, M., 2013. MR diffusion histology and micro-tractography reveal mesoscale features of the human cerebellum. Cerebellum 12, 923–931.

Dyrby, T.B., Baare, W.F., Alexander, D.C., Jelsing, J., Garde, E., Sogaard, L.V., 2011. An ex vivo imaging pipeline for producing high-quality and high-resolution diffusion-weighted imaging datasets. Hum. Brain Mapp. 32, 544–563.

Dyrby, T.B., Innocenti, G.M., Bech, M., Lundell, H., 2018. Validation strategies for the interpretation of microstructure imaging using diffusion MRI. Neuroimage 182, 62–79.

Dyrby, T.B., Sogaard, L.V., Hall, M.G., Ptito, M., Alexander, D.C., 2012. Contrast and stability of the axon diameter index from microstructure imaging with diffusion MRI. Magn. Reson. Med. 70, 711–721.

Eggenschwiler, F., O'Brien, K.R., Gallichan, D., Gruetter, R., Marques, J.P., 2016. 3D T 2-weighted imaging at 7T using dynamic kT-points on single-transmit MRI systems. Magma 29, 347–358.

Eggenschwiler, F., O'Brien, K.R., Gruetter, R., Marques, J.P., 2014. Improving T2 -weighted imaging at high field through the use of kT -points. Magn. Reson. Med. 71, 1478–1488.

Fan, Q., Nummenmaa, A., Polimeni, J.R., Witzel, T., Huang, S.Y., Wedeen, V.J., Rosen, B.R., Wald, L.L., 2017. HIgh b-value and high Resolution Integrated Diffusion (HIBRID) imaging. Neuroimage 150, 162–176.

Fatterpekar, G.M., Naidich, T.P., Delman, B.N., Aguinaldo, J.G., Gultekin, S.H., Sherwood, C.C., Hof, P.R., Drayer, B.P., Fayad, Z.A., 2002. Cytoarchitecture of the human cerebral cortex: MR microscopy of excised specimens at 9.4 Tesla. AJNR Am. J. Neuroradiol. 23, 1313–1321.

Foxley, S., Jbabdi, S., Clare, S., Lam, W., Ansorge, O., Douaud, G., Miller, K., 2014. Improving diffusion-weighted imaging of post-mortem human brains: SSFP at 7 T. Neuroimage 102 Pt 2, 579–589.

Frahm, J., Merboldt, K.D., Hänicke, W., Haase, A., 1985. Stimulated echo imaging. J. Magn. Reson. 64 (1969), 81–93.

Glover, P.M., Bowtell, R.W., Brown, G.D., Mansfield, P., 1994. A microscope slide probe for high resolution imaging at 11.7 Tesla. Magn. Reson. Med. 31, 423–428.

Gudbjartsson, H., Patz, S., 1995. The Rician distribution of noisy MRI data. Magn. Reson. Med. 34, 910–914.

Harms, R.L., Fritz, F.J., Tobisch, A., Goebel, R., Roebroeck, A., 2017. Robust and fast nonlinear optimization of diffusion MRI microstructure models. Neuroimage 155, 82–96.

Jespersen, S.N., Olesen, J.L., Hansen, B., Shemesh, N., 2017. Diffusion time dependence of microstructural parameters in fixed spinal cord. Neuroimage 182, 329–342.

Jones, D.K., Basser, P.J., 2004. Squashing peanuts and smashing pumpkins": how noise distorts diffusion-weighted MR data. Magn. Reson. Med. 52, 979–993.

Kellman, P., McVeigh, E.R., 2005. Image reconstruction in SNR units: a general method for SNR measurement. Magn. Reson. Med. 54, 1439–1447.

Kleinnijenhuis, M., Mollink, J., Lam, W.W., Kinchesh, P., Khrapitchev, A.A., Smart, S.C., Jbabdi, S., Miller, K.L., 2018. Choice of reference measurements affects quantification of long diffusion time behaviour using stimulated echoes. Magn. Reson. Med. 79, 952–959.

Kleinnijenhuis, M., Zerbi, V., Kuster, B., Slump, C.H., Barth, M., van Walsum, A.M.V., 2013. Layer-specific diffusion weighted imaging in human primary visual cortex in vitro. Cortex 49, 2569–2582.

Leergaard, T.B., White, N.S., de Crespigny, A., Bolstad, I., D'Arceuil, H., Bjaalie, J.G., Dale, A.M., 2010. Quantitative histological validation of diffusion MRI fiber orientation distributions in the rat brain. PLoS One 5.

Leuze, C.W., Anwander, A., Bazin, P.L., Dhital, B., Stuber, C., Reimann, K., Geyer, S., Turner, R., 2014. Layer-specific intracortical connectivity revealed with diffusion MRI. Cerebr. Cortex 24, 328–339.

Liang, Z.P., Lauterbur, P.C., 1999. Principles of Magnetic Resonance Imaging: A Signal Processing Perspective. Wiley.

Lundell, H., Alexander, D.C., Dyrby, T.B., 2014. High angular resolution diffusion imaging with stimulated echoes: compensation and correction in experiment design and analysis. NMR Biomed. 27, 918–925.

Lutti, A., Stadler, J., Josephs, O., Windischberger, C., Speck, O., Bernarding, J., Hutton, C., Weiskopf, N., 2012. Robust and fast whole brain mapping of the RF transmit field B1 at 7T. PLoS One 7, e32379.

McNab, J.A., Jbabdi, S., Deoni, S.C., Douaud, G., Behrens, T.E., Miller, K.L., 2009. High resolution diffusion-weighted imaging in fixed human brain using diffusion-weighted steady state free precession. Neuroimage 46, 775–785.

Merboldt, K.D., Hanicke, W., Frahm, J., 1991. Diffusion imaging using stimulated echoes. Magn. Reson. Med. 19, 233–239.

Miller, D.J., Duka, T., Stimpson, C.D., Schapiro, S.J., Baze, W.B., McArthur, M.J., Fobbs, A.J., Sousa, A.M., Sestan, N., Wildman, D.E., Lipovich, L., Kuzawa, C.W., Hof, P.R., Sherwood, C.C., 2012a. Prolonged myelination in human neocortical evolution. Proc. Natl. Acad. Sci. U. S. A. 109, 16480–16485.

Miller, K.L., McNab, J.A., Jbabdi, S., Douaud, G., 2012b. Diffusion tractography of post-mortem human brains: optimization and comparison of spin echo and steady-state free precession techniques. Neuroimage 59, 2284–2297.

Miller, K.L., Stagg, C.J., Douaud, G., Jbabdi, S., Smith, S.M., Behrens, T.E., Jenkinson, M., Chance, S.A., Esiri, M.M., Voets, N.L., Jenkinson, N., Aziz, T.Z., Turner, M.R., Johansen-Berg, H., McNab, J.A., 2011. Diffusion imaging of whole, post-mortem human brains on a clinical MRI scanner. Neuroimage 57, 167–181.

Mollink, J., Kleinnijenhuis, M., Cappellen van Walsum, A.V., Sotiropoulos, S.N., Cottaar, M., Mirfin, C., Heinrich, M.P., Jenkinson, M., Pallebage-Gamarallage, M., Ansorge, O., Jbabdi, S., Miller, K.L., 2017. Evaluating fibre orientation dispersion in white matter: comparison of diffusion MRI, histology and polarized light imaging. Neuroimage 157, 561–574.

Nabuurs, R.J., Hegeman, I., Natte, R., van Duinen, S.G., van Buchem, M.A., van der Weerd, L., Webb, A.G., 2011. High-field MRI of single histological slices using an inductively coupled, self-resonant microcoil: application to ex vivo samples of patients with Alzheimer's disease. NMR Biomed. 24, 351–357.

Nehrke, K., Bornert, P., 2012. DREAM–a novel approach for robust, ultrafast, multislice B(1) mapping. Magn. Reson. Med. 68, 1517–1526.

Pfefferbaum, A., Sullivan, E.V., Adalsteinsson, E., Garrick, T., Harper, C., 2004. Postmortem MR imaging of formalin-fixed human brain. Neuroimage 21, 1585–1595.

Pfeuffer, J., Van de Moortele, P.F., Ugurbil, K., Hu, X., Glover, G.H., 2002. Correction of physiologically induced global off-resonance effects in dynamic echo-planar and spiral functional imaging. Magn. Reson. Med. 47, 344–353.

Roebroeck, A., Galuske, R., Formisano, E., Chiry, O., Bratzke, H., Ronen, I., Kim, D.S., Goebel, R., 2008. High-resolution diffusion tensor imaging and tractography of the human optic chiasm at 9.4 T. Neuroimage 39, 157–168.

Roebroeck, A., Miller, K.L., Aggarwal, M., 2018. Ex vivo diffusion MRI of the human brain: technical challenges and recent advances. NMR Biomed., e3941

Roebroeck, A., Sengupta, S., Bastiani, M., Schillak, S., Tramm, B., Waks, M., Lataster, A., Herrler, A., Tse, D.H., Poser, B.A., 2015. High Resolution MRI Neuroanatomy of the Whole Human Brain Post Mortem with a Specialized 9.4T RF-Coil. OHBM, Honolulu (HW, USA).

Seehaus, A., Roebroeck, A., Bastiani, M., Fonseca, L., Bratzke, H., Lori, N., Vilanova, A., Goebel, R., Galuske, R., 2015. Histological validation of high-resolution DTI in human post mortem tissue. Front. Neuroanat. 9.

Seehaus, A.K., Roebroeck, A., Chiry, O., Kim, D.S., Ronen, I., Bratzke, H., Goebel, R., Galuske, R.A., 2013. Histological validation of DW-MRI tractography in human postmortem tissue. Cerebr. Cortex 23, 442–450.

Sengupta, S., Fritz, F.J., Harms, R.L., Hildebrand, S., Tse, D.H.Y., Poser, B.A., Goebel, R., Roebroeck, A., 2018. High resolution anatomical and quantitative MRI of the entire human occipital lobe ex vivo at 9.4T. Neuroimage 168, 162–171.

Setsompop, K., Wald, L.L., Alagappan, V., Gagoski, B.A., Adalsteinsson, E., 2008. Magnitude least squares optimization for parallel radio frequency excitation design demonstrated at 7 Tesla with eight channels. Magn. Reson. Med. 59, 908–915.

Sotiropoulos, S.N., Jbabdi, S., Andersson, J.L., Woolrich, M.W., Ugurbil, K., Behrens, T.E., 2013. RubiX: combining spatial resolutions for Bayesian inference of crossing fibers in diffusion MRI. IEEE Trans. Med. Imaging 32, 969–982.

St-Jean, S., Coupe, P., Descoteaux, M., 2016. Non Local Spatial and Angular Matching: enabling higher spatial resolution diffusion MRI datasets through adaptive denoising. Med. Image Anal. 32, 115–130.

Sun, S.W., Neil, J.J., Liang, H.F., He, Y.Y., Schmidt, R.E., Hsu, C.Y., Song, S.K., 2005. Formalin fixation alters water diffusion coefficient magnitude but not anisotropy in infarcted brain. Magn. Reson. Med. 53, 1447–1451.

Tamir, J.O., F, Cheng, J.Y., Uecker, M., Lustig, M., 2016. Generalized Magnetic Resonance Image Reconstruction Using the Berkeley Advanced Reconstruction Toolbox. ISMRM Workshop on Data Sampling and Image Reconstruction, Sedona.

Triantafyllou, C., Polimeni, J.R., Wald, L.L., 2011. Physiological noise and signal-to-noise ratio in fMRI with multi-channel array coils. Neuroimage 55, 597–606.

Tse, D.H., Wiggins, C.J., Ivanov, D., Brenner, D., Hoffmann, J., Mirkes, C., Shajan, G., Scheffler, K., Uludag, K., Poser, B.A., 2016. Volumetric imaging with homogenised excitation and static field at 9.4 T. Magma 29, 333–345.

Uecker, M., Lai, P., Murphy, M.J., Virtue, P., Elad, M., Pauly, J.M., Vasanawala, S.S., Lustig, M., 2014. ESPIRiT–an eigenvalue approach to autocalibrating parallel MRI: where SENSE meets GRAPPA. Magn. Reson. Med. 71, 990–1001.

Utz, M., Monazami, R., 2009. Nuclear magnetic resonance in microfluidic environments using inductively coupled radiofrequency resonators. J. Magn. Reson. 198, 132–136.

Van Essen, D.C., Jbabdi, S., Sotiropoulos, S.N., Chen, C., Dikranian, K., Coalson, T., Harwell, J., Behrens, T.E.J., Glasser, M.F., 2014. Chapter 16 - mapping connections in humans and non-human primates: aspirations and challenges for diffusion imaging. In: Johansen-Berg, H., Behrens, T.E.J. (Eds.), Diffusion MRI, second ed. Academic Press, San Diego, pp. 337–358.

Veraart, J., Novikov, D.S., Christiaens, D., Ades-Aron, B., Sijbers, J., Fieremans, E., 2016. Denoising of diffusion MRI using random matrix theory. Neuroimage 142, 394–406.

Westin, C.F., Maier, S.E., Mamata, H., Nabavi, A., Jolesz, F.A., Kikinis, R., 2002. Processing and visualization for diffusion tensor MRI. Med. Image Anal. 6, 93–108.

Zhang, H., Dyrby, T.B., Alexander, D.C., 2011. Axon diameter mapping in crossing fibers with diffusion MRI. Med. Image Comput. Comput. Assist. Interv. 14, 82–89.